Research Square

Preprints are preliminary reports that have not undergone peer review.
They should not be considered conclusive, used to inform clinical practice,
or referenced by the media as validated information.

A model for the decay of TKE in the CBL from the time evolution of the length and velocity scales: application in a Eulerian dispersion model

Antonio Goulart

antonio.goulart@furg.br

Universidade Federal do Rio Grande (FURG)

Jonas da Costa Carvalho

Universidade Federal de Pelotas (UFPEL)

Matheus Jatkoske Lazo

Universidade Federal do Rio Grande (FURG)

Julian Moises Sejje Suarez

Universidade Federal do Rio Grande (FURG)

Research Article

Keywords: Convective boundary layer, Turbulence decay, Turbulent kinetic energy, Eddy diffusivity, Sunset transition, Eulerian dispersion model

Posted Date: September 2nd, 2026

DOI: https://doi.org/10.21203/rs.3.rs-10501887/v1

License: This work is licensed under a Creative Commons Attribution 4.0 International License.
Read Full License

Additional Declarations: No competing interests reported.

A model for the decay of TKE in the CBL from the time evolution of the length and velocity scales: application in a Eulerian dispersion model

A. Goulart[1*], J. C. Carvalho[2], M. J. Lazo[1], J. M. S. Suarez[1]

[1*]Instituto de Matemática, Estatísitica and Física, Universidade Federal do Rio Grande (FURG), Rio Grande, 96203-900, RS, Brazil.
[2]Faculdade de Meteorologia, Universidade Federal de Pelotas (UFPEL), Pelotas, 96010-610, RS, Brazil.

*Corresponding author(s). E-mail(s): antonio.goulart@furg.br;
Contributing authors: jonas.carvalho@ufpel.edu.br;
matheuslazo@furg.br; julian.sejje@furg.br;

Abstract

A simple model for the decay of the turbulent kinetic energy (TKE) in the convective boundary layer (CBL) during the afternoon–sunset transition is proposed. Differently from the classical approaches, which are based on the solution of the dynamical equation for the energy density spectrum subject to initial and boundary conditions, the decay is described here through the time evolution of the characteristic scales of the convective flow, namely the convective velocity scale $w_*(t)$ and the inversion height $z_i(t)$, driven by the decreasing surface heat flux. The evolving three-dimensional energy density spectrum is constructed from the one-dimensional convective spectra of Degrazia et al. by means of the spectral tensor formulation of Kristensen et al. for homogeneous non-isotropic turbulence. The main advantage of this new approach is the simplicity of its mathematical formalism, since no differential equation has to be solved. The TKE obtained from the model reproduces well established observational and large-eddy simulation results for the fully developed CBL and, during the decay, agrees closely with the spectral dynamic model obtained from the solution of the dynamical equation for the energy density spectrum. From the evolving spectrum, time- and height-dependent eddy diffusivities for the longitudinal, lateral and vertical directions are derived employing Taylor's statistical diffusion theory. These decaying convective eddy diffusivities are expressed as polynomial functions of the dimensionless height z/z_i for a sequence of dimensionless times t_*, suitable for direct use in air quality models. Differently from the decaying

convective eddy diffusivities of Goulart et al., which are height-independent and derived from the isotropic form of the dynamical equation for the energy density spectrum, the eddy diffusivities proposed here depend explicitly on the height and are supported by a spectral balance equation that retains the buoyancy and the mechanical (shear) production terms. The two sets of eddy diffusivities are incorporated in a Eulerian dispersion model, based on the time-dependent advection–diffusion equation, and compared in two decaying-CBL scenarios: the buoyancy-dominated case of Nieuwstadt and Brost and the shear-and-buoyancy case SB1 of Moeng and Sullivan. In the buoyancy-dominated scenario the two parameterizations produce similar dispersion patterns, whereas in the sheared scenario the height-independent diffusivities strongly underestimate the turbulent transport in the residual layer, showing the advantage of the formulation proposed here when mechanical production is relevant.

Keywords: Convective boundary layer, Turbulence decay, Turbulent kinetic energy, Eddy diffusivity, Sunset transition, Eulerian dispersion model

1 Introduction

The planetary convective boundary layer (CBL) begins to form in the early morning, due to the incidence of solar radiation on the Earth's surface. A well-mixed CBL is reached only in the middle of the day, and it remains approximately quasi-steady for a few hours [1]. In the late afternoon, when the intensity of the solar radiation decreases, the surface heat flux — which is the main forcing sustaining the structure of large vertical thermals that characterizes convective turbulence — progressively weakens, and the CBL enters a process of decay of the kinetic energy of the eddies that form it. Near the ground the heat flux eventually changes sign and a stable boundary layer (SBL) develops, while above it, in the so-called residual layer (RL), the convective energy-containing eddies lose their strength and mixing capacity [2, 3]. During this transition the large eddies are progressively destroyed and the structure of the turbulence changes: the flow becomes increasingly anisotropic and the different scales of motion decay at different rates [4, 5]. It is important to understand the processes involved during the decay of turbulence in this transition period, since the rapid variation of the eddy kinetic energy directly influences the vertical transport of heat, moisture, carbon dioxide and pollutants in the atmosphere [3, 6, 7].

The decay of convective turbulence in the planetary boundary layer has been studied by means of laboratory experiments [8, 9], large-eddy simulations (LES) [4, 10–12], field observations [5, 13–16] and theoretical models [17–19]. In the pioneering LES study of Nieuwstadt and Brost [10] the surface heat flux was abruptly set to zero, and the decay of the turbulent kinetic energy (TKE) was found to scale with the dimensionless time t/τ, where $\tau = z_i/w_*$ is the large-eddy turnover time. Sorbjan [11] considered the more realistic case of a surface heat flux decreasing gradually with time, and showed that the decay is governed by two time scales: the external time scale controlling the changes of the surface flux and the convective time scale; moreover, large eddies were found to persist in the residual layer even after the surface flux becomes

negative. The observations collected during the BLLAST field campaign, and the corresponding LES analyses, confirmed this general picture, showing that the afternoon transition can be divided into distinct phases, with a slow initial decay followed by a faster collapse of the turbulence near the surface, and that the decay rate varies with height and with the eddy scale [5, 20]. In all these studies the decay is mainly related to the decrease of the surface heat flux. In some studies, the delay of the decay of TKE was considered by taking into account the energy source due to wind shear [4, 18, 19].

Both the models employed together with LES [10–12] and the theoretical models [17, 18] that were proposed to describe the decay of TKE in the CBL are based on the solution of a differential equation obtained from the energy balance, subject to certain initial and boundary conditions. In the model of Goulart et al. [17], for instance, the dynamical equation for the three-dimensional energy density spectrum is solved retaining the buoyancy and inertial-transfer terms, and in Goulart et al. [18] the formulation was extended to include the mechanical production term. In this work we consider another way of approaching the problem: the evolution of the turbulent flow during the decay is described as a succession of quasi-stationary states, characterized at each instant by the time evolution of the characteristic scales of the CBL, namely the convective velocity scale $w_*(t)$ and the inversion height $z_i(t)$, whose evolution is driven by the decreasing surface heat flux. One of the advantages of this new approach is the simplicity of its mathematical formalism, since it does not involve the solution of differential equations. This is an important feature from an operational point of view.

The description of the TKE decay is not only of theoretical interest. The decay of the energy-containing eddies in the CBL is the physical mechanism that sustains the dispersion process in the residual layer during the evening transition, when elevated sources release pollutants at heights comparable to, or interacting with, the layer of transition between the growing SBL and the RL [3]. For this purpose, decaying convective eddy diffusivities were derived by Goulart et al. [21] from the isotropic form of the dynamical equation for the energy density spectrum: their expressions depend on the dimensionless time t_* only, being uniform with height, and were employed, for example, in the Lagrangian simulations of the sunset dispersion patterns of Carvalho et al. [3]. In the present work the evolving energy density spectrum obtained from the scale-evolution model is employed, through Taylor's statistical diffusion theory, to derive eddy diffusivities for the decaying CBL that depend on the time *and* on the height, and whose supporting spectral balance equation retains the buoyancy and the mechanical (shear) production terms [18], that is, it describes a non-isotropic decaying turbulence. In this paper, we analyze the differences between these two parameterizations of turbulence in the decaying residual layer—the height-independent isotropic decay expressions of Goulart et al. [21] and the height-dependent expressions proposed here—and their consequences for contaminant dispersion during the sunset transition. To this end, both sets of eddy diffusivities are incorporated in a Eulerian dispersion model, based on the time-dependent advection–diffusion equation, and the simulations are carried out for two decaying-CBL scenarios taken from the LES literature: the buoyancy-dominated case of Nieuwstadt and Brost [10] and the shear-and-buoyancy case SB1 of Moeng and Sullivan [22], in which the mechanical production of turbulence is relevant.

The paper is organized in the following way: in Sect. 2 the model for the decay of the TKE and the derivation of the eddy diffusivities are presented, together with the spectral dynamic model — with buoyancy and shear production — used as reference. In Sect. 3 the model is evaluated against classical observational and large-eddy simulation results, the decaying eddy diffusivities are confronted with those obtained from the spectral dynamic model, the Eulerian dispersion model is described and the simulations of the concentration field during the sunset transition, performed with the eddy diffusivities of this work and with those of Goulart et al. [21] for the two scenarios, are discussed. Finally, Sect. 4 presents the conclusions.

2 The model

2.1 Time evolution of the turbulent kinetic energy

The kinetic energy of the eddies that form a turbulent flow can be estimated from the energy spectrum. The evolution of the kinetic energy of a decaying turbulent flow is considered here to occur continuously in time, as a succession of quasi-stationary states, so that stationary models for the energy spectrum can be employed in each state. The state of the turbulent flow in each instant is described by the characteristic flow scales. To describe the turbulent flow in the different quasi-stationary states we consider the time evolution of the characteristic scales of the CBL, that is, the convective velocity scale w_* and the inversion height z_i. The turbulent kinetic energy (TKE) is given by

$$e\left(z,t\right) = \frac{1}{2}\,\sigma^2\left(z,t\right) = \frac{1}{2}\int_0^\infty E\left(k,z,t\right)\,\mathrm{d}k, \tag{1}$$

where $\sigma^2 = \sigma_u^2 + \sigma_v^2 + \sigma_w^2$ is the sum of the velocity variances, $E(k,z,t)$ is the three-dimensional energy density spectrum (EDS), k is the wavenumber and z is the height above the ground. Since we are considering non-isotropic turbulence, we use the formulation proposed by Kristensen et al. [23]. This formulation allows determining the 3-D spectrum of a homogeneous turbulent flow from the known 1-D spectra, namely

$$\begin{aligned} E\left(k,z,t\right) = k^3\frac{\mathrm{d}}{\mathrm{d}k}\left(\frac{1}{k}\frac{\mathrm{d}E_u(k,z)}{\mathrm{d}k}\right) + 2k^4\int_0^{1/k^2} S^2\,g'''\left(S,z\right)\mathrm{d}S \\ - \frac{14}{9}\,k^{4/3}\int_0^{1/k^2} S^{2/3}\,g'''\left(S,z\right)\mathrm{d}S, \end{aligned} \tag{2}$$

where $E_u(k,z)$ is the one-dimensional longitudinal spectrum, $S = k^{-2}$ is an auxiliary variable and the function $g'''(S,z)$, defined below, is constructed from the three one-dimensional component spectra.

A model for the one-dimensional components of the velocity spectrum in the CBL in a steady state was proposed by Degrazia et al. [24]. The longitudinal component is given by,

$$E_u\,(k,z) = \frac{0.045(\frac{z}{z_i})^{5/3} z_i \psi_\epsilon^{2/3} (f_m)_u^{-5/3} w_*^2}{[1 + 0.24\frac{zk}{(f_m)_u}]^{5/3}}, \tag{3}$$

where

$$\psi_\epsilon = 0.62 \left(\frac{z}{z_i}\right)^{-1/3} \left(1 - \frac{z}{z_i}\right)^{1/4}, \tag{4}$$

$$(f_m)_u = \frac{z}{1.5 z_i}. \tag{5}$$

The dimensionless dissipation function $\psi_\epsilon = \varepsilon\, z_i / w_*^3$ in Eq. (4) is an analytical approximation of the vertical profile of the dimensionless dissipation rate resolved by the large-eddy simulation of the fully developed CBL of Goulart et al. [17] (their Fig. 1), adopted here in place of the surface-layer expression of Højstrup [25] used in the original formulation of Degrazia et al. [24]. The simulated profile decreases monotonically with height and vanishes at the inversion — a behaviour that the surface-layer expression does not capture — and the shape $\propto (z/z_i)^{-1/3}(1 - z/z_i)^{1/4}$ reproduces it with a root-mean-square deviation of about 0.02. Since the dissipation rate of that simulation was computed from the subgrid-scale kinetic energy (Eq. 29 of Goulart et al. [17]), which underestimates the total dissipation, the amplitude in Eq. (4) was rescaled so as to match, at $z/z_i = 0.5$, the value given by the original Højstrup expression for the reference scenario of Sect. 3.3.1. This calibration leaves the turbulence intensity of the central region of the CBL essentially unchanged, while correcting the position of the maximum of the vertical velocity variance and its decay towards the top of the layer (Sect. 3.1.1).

The lateral and vertical components of the Degrazia et al. [24] spectra have the same functional form, so that, in terms of the wavenumber, the three components can be written compactly as

$$E_i\,(k,z) = \frac{a_i}{(1 + b_i k)^{5/3}}, \qquad i = u, v, w, \tag{6}$$

with

$$a_i = \frac{1.06\, c_i}{2\pi} \left(\frac{z}{z_i}\right)^{5/3} z_i\, \psi_\epsilon^{2/3}\, (f_m)_i^{-5/3}\, w_*^2, \qquad b_i = \frac{1.5}{2\pi}\, \frac{z}{(f_m)_i}, \tag{7}$$

where $c_i = \alpha_i \alpha_u (2\pi\kappa)^{-2/3}$, with $\alpha_u = 0.5 \pm 0.05$, $\kappa = 0.4$ and $\alpha_i = 1, 4/3, 4/3$ for the u, v and w components, so that $c_u = 0.27$ and $c_v = c_w = 0.36$ [24]; $(f_m)_v = (f_m)_u$ is given by (5) and $(f_m)_w$ by Eq. (20) of Sect. 2.2. For $i = u$, Eq. (6) recovers the expression (3).

The term $g'''(S,z)$ in Eq. (2) is obtained from the one-dimensional spectra (6) following the procedure of Kristensen et al. [23]. Introducing the variable $S = k^{-2}$ and defining

$$f_i\,(S,z) = S^2\, E_i\left(S^{-1/2}, z\right) = \frac{A_i\, S^{17/6}}{\left(1 + \sqrt{B_i S}\right)^{5/3}}, \qquad A_i = a_i\, b_i^{-5/3}, \qquad B_i = b_i^{-2}, \tag{8}$$

the function $g'''(S,z)$ is given by the combination

$$g'''(S,z) = \sum_{i=u,v,w} m_i\, f_i'''(S,z)\,, \qquad m_u = 2, \qquad m_v = m_w = -1, \tag{9}$$

where the third derivative of (8) with respect to S has the closed form

$$f_i'''(S,z) = A_i \sum_{n=0}^{3} C_n\, B_i^{\frac{3-n}{2}}\, \frac{S^{\frac{8-3n}{6}}}{\left(1+\sqrt{B_i S}\right)^{\frac{14-3n}{3}}}, \tag{10}$$

with

$$C_0 = -\frac{55}{27}, \qquad C_1 = \frac{70}{9}, \qquad C_2 = -\frac{725}{72}, \qquad C_3 = \frac{935}{216}. \tag{11}$$

With Eqs. (9)–(11), the integrals in Eq. (2) can be reduced to a closed algebraic form; the derivation is presented in Appendix B.

For expression (2) to represent the time evolution of the energy spectrum, we consider the time evolution of the characteristic flow scales in the CBL, that is, the convective velocity scale $w_*(t)$ and the inversion height $z_i(t)$. For the inversion height we consider the following expression,

$$z_i\,(t) = z_i(t_0)\left[\cos\left(\frac{\pi}{2}\,\frac{t}{\tau_f}\right)\right]^{1/2}, \tag{12}$$

where $z_i(t_0)$ is the inversion height at the onset of the decay. Expression (12) follows from the encroachment relation between the mixed-layer depth and the accumulated surface buoyancy input [26], particularised to the decaying regime in which the layer depth adjusts quasi-statically to the instantaneous surface heat flux; writing it normalised by $z_i(t_0)$ absorbs the proportionality constant and the potential-temperature gradient γ_0 above the mixed layer into the initial height, so that no scenario-dependent constant is carried explicitly. The surface virtual temperature flux is denoted $\overline{(w\theta)}_0(t)$. An expression for the convective velocity scale as a function of time is obtained from its definition [27, 28],

$$w_*(t) = \left(\frac{g}{\theta}\, z_i(t)\, \overline{(w\theta)}_0(t)\right)^{1/3}, \tag{13}$$

where g/θ is the buoyancy parameter.

The time evolution of $w_*(t)$ and $z_i(t)$ occurs due to the evolution in time of the surface heat flux. Following Sorbjan [11], the surface heat flux is assumed to decrease in time according to

$$\overline{(w\theta)}_0(t) = \overline{(w\theta)}_0(t_0)\, \cos\left(\frac{\pi}{2}\,\frac{t}{\tau_f}\right), \tag{14}$$

where $\overline{(w\theta)}_0(t_0)$ is the surface heat flux at $t = t_0$, τ_f is the external time scale controlling the temporal variation of the surface heat flux, and $t = t_0$ is the instant of time when the TKE begins to decay in the CBL. The relevant dimensionless time during the decay is $t_* = t/\tau$, where $\tau = z_i/w_*$ is the large-eddy turnover time evaluated at

$t = t_0$ [10, 11]. Substituting the expressions (2)–(14) into (1) gives an expression for the TKE as a function of time.

According to Eqs. (12)–(14), the surface heat flux, the inversion height and the convective velocity scale all decrease as the sunset transition proceeds, with $z_i(t) \propto \cos^{1/2}(\pi t/2\tau_f)$ and $w_*(t) \propto \cos^{1/2}(\pi t/2\tau_f)$. As a consequence, the product $w_*(t)\, z_i(t)$ and the turbulent kinetic energy, $e \propto w_*^2 \propto \cos(\pi t/2\tau_f)$, decay together with the surface forcing and vanish at the dimensionless time $t_* = \tau_f w_*/z_i \approx 5.3$. This describes the progressive shrinking of the layer occupied by the active convective eddies as the buoyant forcing weakens, and the formation of a residual layer above the shrinking mixed layer, in which the energy-containing eddies inherited from the daytime CBL lose their strength and mixing capacity. The inversion height at the onset of the decay, $z_i(t_0)$, is prescribed by the scenario considered (Sect. 3.3).

2.2 Eddy diffusivities for the decaying convective turbulence

For application in pollutant dispersion models during the decay of the convective turbulence, expressions for the eddy diffusivities are necessary. Whether the dispersion is described by a Lagrangian stochastic particle model [3] or by a Eulerian model based on the advection–diffusion equation with first-order (gradient-transfer) closure, as considered in this work (Sect. 3.2), the turbulent transport is represented by the eddy diffusivities.

The eddy diffusivity can be obtained from the following relation [29]

$$K_i = \sigma_i^2\, T_{L,i}, \tag{15}$$

where [24]

$$T_{L,i} = \frac{\beta_i E_i(0,z)}{4\sigma_i^2} \tag{16}$$

is the Lagrangian decorrelation time scale, $\beta_i = 0.55\, U/\sigma_i$ is the ratio of the Lagrangian to the Eulerian time scales [30], U is the component of the wind speed in the x-direction and $E_i(0,z)$ is the 1-D Eulerian energy spectrum evaluated at $n = 0$. Substituting (16) into (15) we obtain the following expression for the eddy diffusivity,

$$K_\gamma = \frac{0.55}{4}\, \frac{U E_j(0,z)}{\sigma_j}, \qquad \gamma = x, y, z \qquad \text{and} \qquad j = u, v, w. \tag{17}$$

To obtain the components of the eddy diffusivity the components of the energy spectrum are required. We consider the spectra of Degrazia et al. [24] already employed in Sect. 2.1, now written as a function of the frequency n,

$$E_j(n,z) = \frac{1.06 c_j \frac{z}{U}\, \psi_\epsilon^{2/3} (\frac{z}{z_i})^{2/3} (f_m)_j^{-5/3} w_*^2}{[1 + \frac{1.5 \frac{nz}{U}}{(f_m)_j}]^{5/3}} \quad j = u, v, w, \tag{18}$$

where $c_u = 0.27$, $c_v = c_w = 0.36$; in terms of the wavenumber $k = 2\pi n/U$, Eq. (18) recovers the form (6). Furthermore,

$$(f_m)_v = \frac{z}{1.5 z_i} \tag{19}$$

$$(f_m)_w = \frac{z}{1.8 z_i [1 - \exp(-4\frac{z}{z_i}) - 0.0003 \exp(8\frac{z}{z_i})]} \tag{20}$$

To calculate σ_j in (17), we consider the definition of the velocity variance,

$$\sigma_j^2 (z) = \int_0^\infty E_j (n, z) \, \mathrm{d}n, \tag{21}$$

From (21) and (18) we obtain,

$$\sigma_j(z) = (1.06\, c_j)^{1/2} \, \psi_\epsilon^{1/3} \Big(\frac{z}{z_i}\Big)^{1/3} (f_m)_j^{-1/3} \, w_*. \tag{22}$$

Replacing (22) and (18) (with $n = 0$) in (17), already considering the convective velocity scale and the inversion height as functions of time, we get

$$K_\gamma (z, t) = \frac{0.55}{4} (1.06\, c_j)^{1/2} \, w_*(t) \, z_i(t) \, \psi_\epsilon^{1/3} \Big(\frac{z}{z_i(t)}\Big)^{4/3} (f_m)_j^{-4/3}, \tag{23}$$

which coincides with the convective limit of the eddy diffusivity derived by Degrazia et al. [24] (their Eq. 15). Explicitly, the three components are

$$K_x (z, t) = 0.074 \, w_*(t) \, z_i(t) \, \psi_\epsilon^{1/3} \Big(\frac{z}{z_i(t)}\Big)^{4/3} (f_m)_u^{-4/3}, \tag{24}$$

$$K_y (z, t) = 0.085 \, w_*(t) \, z_i(t) \, \psi_\epsilon^{1/3} \Big(\frac{z}{z_i(t)}\Big)^{4/3} (f_m)_v^{-4/3}, \tag{25}$$

$$K_z (z, t) = 0.085 \, w_*(t) \, z_i(t) \, \psi_\epsilon^{1/3} \Big(\frac{z}{z_i(t)}\Big)^{4/3} (f_m)_w^{-4/3}. \tag{26}$$

The eddy diffusivities (24)–(26) depend on time through $w_*(t)$ and $z_i(t)$ and on height through the dissipation function ψ_ϵ and the reduced frequencies of the spectral peaks $(f_m)_j$; convenient polynomial fits of the vertical profiles of K_x, K_y and K_z, evaluated at a sequence of dimensionless times t_*, are presented in Appendix A.

2.3 The spectral dynamic model

In order to assess the eddy diffusivities obtained from the scale-evolution model, we also consider the classical dynamic approach [17, 18, 21], in which the decay is obtained from the solution of the differential equation for the three-dimensional energy density spectrum $E(k, t, z)$ derived from the spectral energy balance. Retaining the buoyancy production term, the mechanical (shear) production term in the parameterized form

of Goulart et al. [18], the inertial energy transfer parameterized following Pao [31] and the molecular dissipation, the balance equation reads, in dimensionless form ($k' = k z_i$, $t_* = t w_*/z_i$, $E' = E/w_*^2 z_i$, with w_* and z_i evaluated at $t = t_0$),

$$\frac{\partial E'}{\partial t_*} + D(k')\,\frac{\partial E'}{\partial k'} + G(k')\,E' = S_b(k')\cos(B t_*) + M(k'), \tag{27}$$

with

$$D(k') = \alpha_K^{-1}\,\psi_\varepsilon^{1/3}\,k'^{5/3} + c_2\,\psi_\varepsilon^{2/3}\,k'^{1/3}, \tag{28}$$

$$G(k') = \frac{\mathrm{d}D}{\mathrm{d}k'} + \frac{2}{Re}\,k'^2, \tag{29}$$

$$S_b(k') = c_1\,\frac{w_* z_i}{\overline{(w\theta)}_0(t_0)}\,\gamma_c\,\psi_\varepsilon^{-1/3}\,k'^{-2/3}\,E_0'(k'), \tag{30}$$

$$M(k') = c_m\,\frac{\phi_m\,\phi_\varepsilon^{-1/3}\,u_*^2}{(\kappa z)^{2/3}}\,\frac{z_i^{2/3}}{w_*^{2/3}}\,k'^{-2/3}\,E_0'(k'), \tag{31}$$

where $\alpha_K = 1.5$ is the Kolmogorov constant, $\psi_\varepsilon(z/z_i)$ is the dimensionless dissipation function of Eq. (4), γ_c is the vertical gradient of potential temperature inside the mixed layer, $Re = w_* z_i/\nu$ is the Reynolds number (ν being the kinematic viscosity), $B = (\pi/2)\,z_i/(w_*\tau_f)$ expresses the decrease of the surface heat flux (Eq. 14) in dimensionless time and $\kappa = 0.4$ is the von Kármán constant. The functions ϕ_m and ϕ_ε are the Monin–Obukhov similarity functions for the wind shear and for the dissipation rate; in the unstable surface layer the Businger–Dyer form $\phi_m = (1 - 15\,z/L)^{-1/4}$ is adopted, with $L = u_*^3/[\kappa\,(g/\theta)\,\overline{(w\theta)}_0(t_0)]$ the Obukhov length.

The functions $c_1(z/z_i)$ and $c_2(z/z_i)$ and the constant c_m are not free parameters: they are fixed by the requirement that the fully developed CBL be a stationary state of Eq. (27), following the procedure of Goulart et al. [17, 21]. The function c_1 follows from imposing that the wavenumber-integrated buoyancy source reproduce the convective production of the TKE budget of Moeng and Sullivan [22], $\int_0^\infty S_b(k')\,\mathrm{d}k' = 1 - 1.2\,z/z_i$, which gives

$$c_1\!\left(\frac{z}{z_i}\right) = \frac{1 - 1.2\,z/z_i}{\dfrac{w_* z_i}{\overline{(w\theta)}_0(t_0)}\,\gamma_c\,\psi_\varepsilon^{-1/3}\displaystyle\int_0^\infty k'^{-2/3} E_0'(k')\,\mathrm{d}k'}, \tag{32}$$

and c_2, which scales the convective contribution to the spectral transfer velocity, follows from matching the same production to the maximum of the transfer term,

$$c_2\!\left(\frac{z}{z_i}\right) = \frac{1 - 1.2\,z/z_i}{\psi_\varepsilon^{2/3}\,\max_{k'}\left[\,k'^{1/3} E_0'(k')\,\right]}. \tag{33}$$

Equations (32)–(33) are evaluated numerically at each height with the three-dimensional spectrum E_0' of Eq. (2); representative values are $c_1 = 0.32$, 0.22, 0.12 and 0.014 and $c_2 = 8.3$, 8.5, 6.6 and 1.2 at $z/z_i = 0.1$, 0.25, 0.5 and 0.8, respectively. The calibration is restricted to $0.05 \le z/z_i \le 0.80$, since the convective production

of Moeng and Sullivan [22] changes sign at $z/z_i = 0.833$. The constant c_m, in turn, never has to be evaluated: because the buoyant and the mechanical sources share the same spectral shape $k'^{-2/3}E'_0(k')$, their sum at $t = t_0$ is completely determined by the stationarity condition stated below, and the only quantity that remains to be prescribed is the *fraction* of the total production that is mechanical, $r(z)$, defined in the next paragraph. No constant of the dynamic model is therefore adjusted to the decay data. Following Goulart et al. [18], the buoyancy source decays with the surface heat flux, whereas the mechanical source (31) is stationary in time, since the surface stress does not vanish with the solar forcing; both share the spectral form $k'^{-2/3}E'_0(k')$. The relative weight of the two sources is fixed by the ratio of the corresponding production terms of the TKE budget of Moeng and Sullivan [22], $r(z) = P_s/(P_s + P_b)$ with $P_b = (g/\theta)\,\overline{(w\theta)}_0(t_0)\,(1 - 1.2\,z/z_i)$ and $P_s = u_*^3(1 - z/z_i)\,\phi_m/(\kappa z)$, so that the total source can be written as $S(k')\,[\,(1 - r)\cos(Bt_*) + r\,]$. For the buoyancy-dominated scenario of Nieuwstadt and Brost [10] ($u_*/w_* \approx 0.11$) one finds $r \lesssim 0.3\%$ in the core of the CBL, and the shear term is negligible; for the sheared scenario SB1 of Moeng and Sullivan [22] ($u_*/w_* \approx 0.63$), however, r reaches 0.45–0.8, and the mechanical term controls the late stages of the decay (Sect. 3.3). The initial condition E'_0 is the three-dimensional CBL spectrum of Degrazia et al. [24], Eq. (2), the same spectrum that feeds the scale-evolution model, and the total source at $t = t_0$ is determined so that E'_0 is a stationary solution of Eq. (27) — the fully developed CBL represented as a source–sink equilibrium. Equation (27) is hyperbolic of first order in (t_*, k') and is solved exactly by the method of characteristics, advancing the solution along the coordinate $\xi(k') = \int \mathrm{d}k'/D(k')$, in which the spectral advection has unit velocity.

The one-dimensional component spectra required to evaluate the eddy diffusivities are recovered from the evolving three-dimensional spectrum by means of the weight-function relation introduced by Goulart et al. [21] (their Eq. 19) and employed by Goulart et al. [18] (their Eq. 24),

$$F_j(k,t,z) = \alpha(k)\,\frac{\dfrac{1}{T}\displaystyle\int_0^t F_j(k,t',z)\,\mathrm{d}t'}{\dfrac{1}{T}\displaystyle\int_0^t E(k,t',z)\,\mathrm{d}t'}\,E(k,t,z), \qquad j = u, w, \tag{34}$$

in which the ratio of the two time integrals — T being the averaging period, which cancels in the ratio — is a weight function that measures the fraction of the three-dimensional energy carried by the component j at wavenumber k, and $\alpha(k)$ is a proportionality constant, obtained in Goulart et al. [21] by comparison with the LES data of Nieuwstadt and Brost [10], which gives $\alpha(k) = 1$. Equation (34) is an integral equation for F_j; its solution [18, 21] is

$$F_j(k,t,z) = F_j(k,0,z)\,\exp\left[\int_0^t Q'(k,s,z)\,\mathrm{d}s\right], \tag{35}$$

with

$$Q'(k,s,z) = \alpha(k)\,Q(k,s,z) + \frac{1}{Q(k,s,z)}\frac{\partial Q(k,s,z)}{\partial s}, \qquad Q(k,s,z) = \frac{E(k,s,z)}{\displaystyle\int_0^t E(k,s',z)\,\mathrm{d}s'}. \tag{36}$$

In the present work we adopt the fixed-weight (frozen-fraction) limit of Eqs. (34)–(36), in which the weight function is evaluated once at $t = t_0$ and held constant during the decay,

$$F_j(k,t,z) = \frac{F_j(k,0,z)}{E(k,0,z)}\,E(k,t,z), \tag{37}$$

so that each component retains its initial share of the evolving three-dimensional spectrum. This is the approximation implicitly made whenever the component partition is not itself advanced in time; it amounts to freezing the anisotropy of the flow at its initial value, and is adequate here because the two formulations being compared in Sect. 3.1.2 are projected with the *same* weight function, so that the comparison is insensitive to it. It should be noted, however, that the anisotropy of the CBL does evolve during the afternoon transition [5]: relaxing Eq. (37) to a prognostic partition is a natural refinement of the dynamic reference model, which would not modify the scale-evolution model proposed here. The initial component spectra $F_j(k,0,z)$ are the CBL spectra of Degrazia et al. [24], Eq. (6).

In the dynamic approach the eddy diffusivities are then obtained by applying the same expressions (24)–(26) to the projected component spectra, that is, using $F_j(0,t,z)$ and $\sigma_j^2(z,t) = \int_0^\infty F_j(k,t,z)\,\mathrm{d}k$ obtained from the solution of Eq. (27) followed by the weight-function projection (37). In this way the two formulations differ only in the description of the decay — the solution of the spectral balance equation followed by the weight-function projection in the dynamic model, the time evolution of the characteristic scales in the model proposed in this work — and the comparison between them, presented in Sect. 3.1.2, is not affected by the particular form adopted for the eddy diffusivity.

3 Results and discussion

3.1 Model evaluation

3.1.1 Velocity variances and decaying eddy diffusivities

At $t = t_0$ equation (1) represents the turbulent kinetic energy in the fully developed convective boundary layer. Since the eddy diffusivities of Sect. 2.2 are constructed from the individual spectral components, the model is evaluated here at the level of the component variances rather than of the total TKE. Figure 1 compares the normalized variances obtained from the spectra of Degrazia et al. [24], Eq. (22), at $t = t_0$ with classical convective references. For the vertical component the reference is the empirical profile $\sigma_w^2/w_*^2 = 1.8\,(z/z_i)^{2/3}(1 - 0.8\,z/z_i)^2$ proposed by Lenschow et al. [32] from aircraft measurements, which large-eddy simulation studies have shown to be nearly universal in the CBL [33]. For the horizontal components the reference is

the typical mixed-layer value $\sigma_u^2 \approx \sigma_v^2 \approx 0.3\, w_*^2$ observed by Caughey and Palmer [34]; it should be kept in mind that, unlike the vertical variance, the normalized horizontal variances do not collapse onto a universal profile, being sensitive to wind shear and mesoscale forcing [33]. The model reproduces the structure of the observed profile of the vertical variance. Its maximum, $\sigma_w^2 \approx 0.40\, w_*^2$ at $z/z_i \approx 0.34$, is located at essentially the same height as the maximum of the Lenschow et al. profile ($0.47\, w_*^2$ at $z/z_i \approx 0.31$); in the central region, where the convective transport is most intense and the eddy diffusivities attain their maxima, the two curves remain close ($0.38\, w_*^2$ against $0.41\, w_*^2$ at $z/z_i = 0.5$), and towards the top of the layer the model variance decays with the dissipation function (4), vanishing at $z = z_i$ as suggested by the data. The horizontal variances cross the observed mixed-layer level in the core of the CBL ($\sigma_u^2 \approx 0.28\, w_*^2$ at $z/z_i = 0.5$; σ_v^2 is larger by the factor 4/3 of the lateral spectral constant c_v) and, unlike the constant reference value, decrease with height — a height dependence that cannot be assessed against a universal profile, since the normalized horizontal variances are known not to collapse [33]. The remaining limitations are quantitative rather than structural: the amplitude of the σ_w^2 maximum is about 15% below the empirical profile, and in the upper part of the layer ($z/z_i \gtrsim 0.8$) the decay of the model variances is somewhat slower than that of the observations (e.g. $0.20\, w_*^2$ against $0.13\, w_*^2$ at $z/z_i = 0.9$).

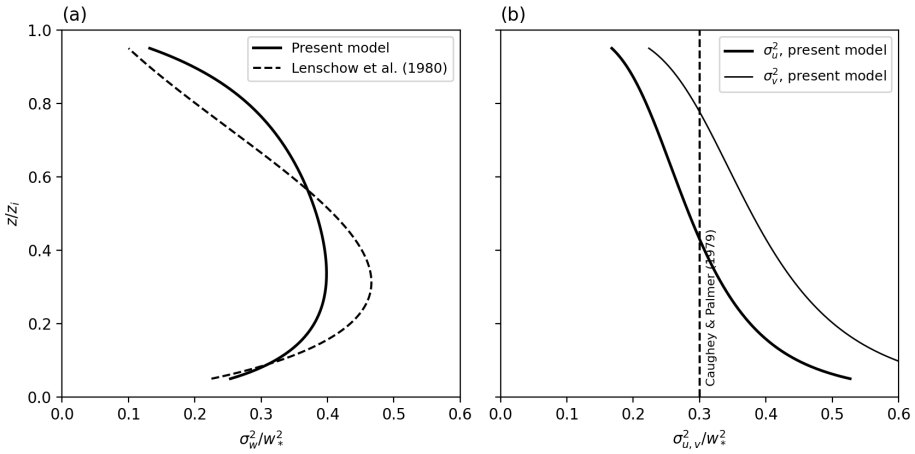


Fig. 1 Normalized velocity variances at $t = t_0$ calculated from the spectra of Degrazia et al. [24], Eq. (22), for the reference scenario of Sect. 3.3.1. (a) Vertical component: the solid line is the model and the dashed line is the empirical profile $1.8\,(z/z_i)^{2/3}(1 - 0.8\, z/z_i)^2$ of Lenschow et al. [32]. (b) Horizontal components: the black and grey solid lines are the model σ_u^2 and σ_v^2; the dashed vertical line marks the typical mixed-layer value $0.3\, w_*^2$ reported by Caughey and Palmer [34].

Figures 2, 3 and 4 show the evolution in time of the components of the eddy diffusivity in the x, y and z directions, respectively, as functions of the height normalized by the height of the convective boundary layer. It is possible to see that the eddy diffusivity decreases in intensity over time at all heights. This is a consequence of the

decrease of the turbulent kinetic energy over time. It is worth noting that the vertical component (Figure 4) retains the characteristic convective shape, with a maximum in the middle of the CBL, while its magnitude decreases as the energy-containing eddies decay, in agreement with the behaviour of the decaying convective eddy diffusivities derived by Goulart et al. [21].

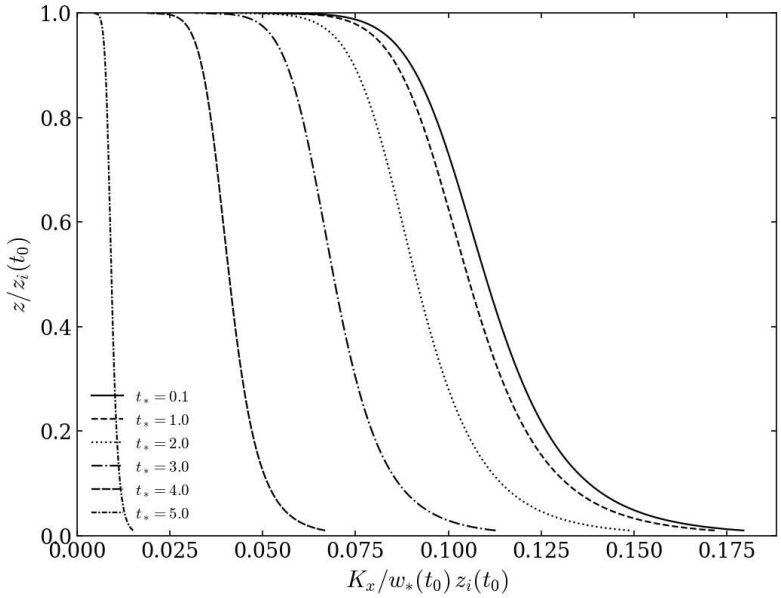


Fig. 2 Temporal evolution of the vertical profiles of the longitudinal eddy diffusivity K_x, normalized by the initial value $w_*(t_0)\,z_i(t_0)$, as a function of the dimensionless height $z/z_i(t_0)$. The profiles are evaluated at six dimensionless times, $t_* = 0.1$, 1.0, 2.0, 3.0, 4.0 and 5.0.

3.1.2 Comparison with the spectral dynamic model

To test the capability of our model to describe the decay of the TKE we confront it with the spectral dynamic model described in Sect. 2.3, in which the turbulent kinetic energy is obtained from the solution of the dynamical equation for the energy density spectrum derived from the spectral energy balance [17, 21]. To isolate the effect of the two descriptions of the decay, both models are integrated from the same initial three-dimensional spectrum, constructed from the convective spectra of Degrazia et al. [24], and use the micrometeorological parameters from two different scenarios: the buoyancy-dominated scenario (Section 3.3.1) and the shear-and-buoyancy scenario (Section 3.3.2). Figure 5 shows, for the buoyancy-dominated scenario, the decay of the mean TKE in the central region of the CBL ($0.2 \leq z/z_i \leq 0.8$): the two formulations produce practically the same result, decaying together with the surface heat flux and vanishing at $t_* \approx 5.3$. This agreement occurs because both the dynamic model, obtained from the spectral energy balance equation, and the scale-evolution model

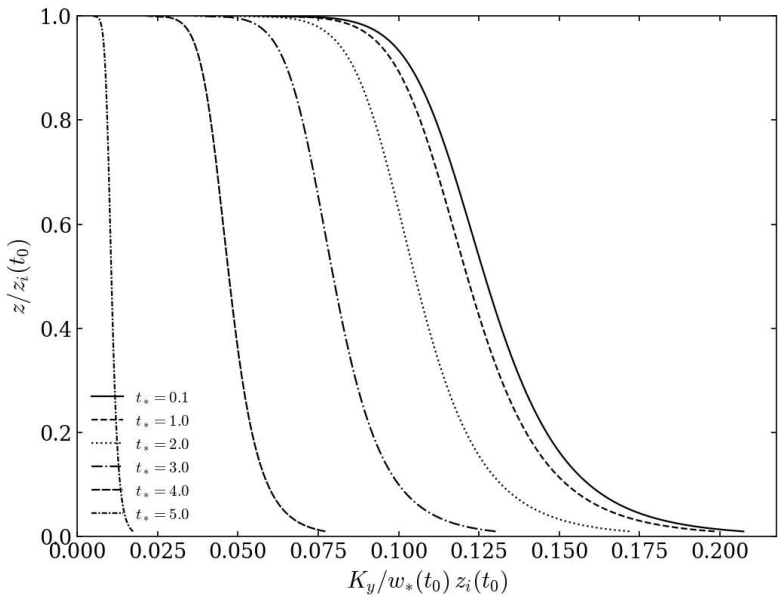


Fig. 3 Temporal evolution of the vertical profiles of the lateral eddy diffusivity K_y, normalized by the initial value $w_*(t_0)\,z_i(t_0)$, as a function of the dimensionless height $z/z_i(t_0)$. The profiles are evaluated at six dimensionless times, $t_* = 0.1$, 1.0, 2.0, 3.0, 4.0 and 5.0.

presented in this work adequately describe the evolution of all the scales involved in the process. A major advantage of the scale-evolution model over the dynamic model is the simplicity of its mathematical formalism, since it does not require the solution of any differential equation, which is important from an operational point of view.

The comparison of Fig. 5 showed that the scale-evolution model and the dynamic model produce equivalent descriptions of the decay of the TKE. Since the quantities that effectively drive the dispersion calculations are the eddy diffusivities, it is important to verify whether this equivalence also holds at the level of K_x and K_z. For this purpose, the eddy diffusivities were computed from both formulations using the same expressions (24)–(26): in the scale-evolution model through the time evolution of $w_*(t)$, $z_i(t)$ and of the variances and length scales, and in the dynamic model through the projected component spectra $F_j(0,t,z)$ and $\sigma_j(z,t)$ obtained from the solution of Eq. (27) followed by the weight-function projection (37), as described in Sect. 2.3. To be consistent with the dispersion simulations of Sect. 3.3, both models employ the micrometeorological parameters of the LES of a decaying CBL of Nieuwstadt and Brost [10]: $z_i = 1350$ m, $w_* = 2.3\,\mathrm{m\,s^{-1}}$ and $u_* = 0.26\,\mathrm{m\,s^{-1}}$, from which $\overline{(w\theta)}_0(t_0) = w_*^3\theta/(g\,z_i) \approx 0.28\ \mathrm{K\,m\,s^{-1}}$; the external time scale is $\tau_f = 3100$ s and the potential temperature gradient in the buoyancy source of Eq. (30) is $\gamma_c = 0.001\ \mathrm{K\,m^{-1}}$. The mechanical source (31) is retained in all the calculations; for this buoyancy-dominated scenario its weight is $r \lesssim 0.3\%$ and its effect on the eddy diffusivities is smaller than $1\ \mathrm{m^2\,s^{-1}}$.

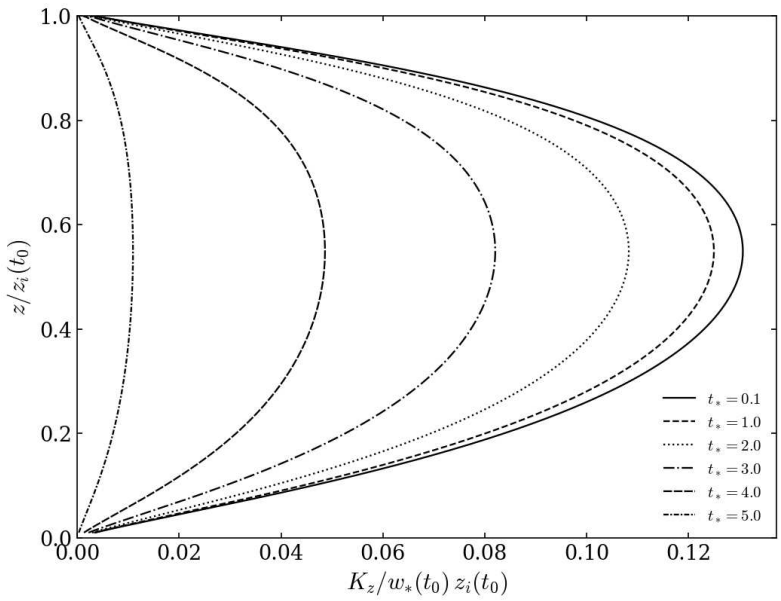


Fig. 4 Temporal evolution of the vertical profiles of the vertical eddy diffusivity K_z, normalized by the initial value $w_*(t_0)\,z_i(t_0)$, as a function of the dimensionless height $z/z_i(t_0)$. The profiles are evaluated at six dimensionless times, $t_* = 0.1$, 1.0, 2.0, 3.0, 4.0 and 5.0. The vertical component retains the characteristic convective shape, with a maximum in the middle of the CBL, while its amplitude decays with the surface heat flux.

Figure 6 shows the temporal evolution of K_x and K_z at $z/z_i = 0.5$ and Fig. 7 the vertical profiles at four dimensionless times; Table 1 presents the corresponding values at three heights. In Table 1 (as in Table 2 of Sect. 3.3.2) the closed forms (24)–(26) of the scale-evolution model are evaluated at fixed heights $z = (z/z_i)\,z_i(t_0)$, with the inversion height shrinking according to Eq. (12); this differs from the frozen-shape operational treatment of Appendix A, in which the profiles retain the convective shape in $z/z_i(t_0)$, by a few percent in the core of the layer and by up to about 13% at $z/z_i = 0.7$ and $t_* = 2.2$. At $t_* = 0$ the two formulations coincide by construction, since they share the initial spectra and the expressions for the eddy diffusivities. The initial spectra of Degrazia et al. [24] are, moreover, taken as a stationary solution of the spectral balance equation (27) at $t = t_0$, the calibration functions $c_1(z/z_i)$ and $c_2(z/z_i)$ being determined for these spectra following the procedure of Goulart et al. [17, 21], so that the fully developed CBL is represented as a source–sink equilibrium and no spurious adjustment transient appears at the beginning of the decay. As the surface heat flux weakens, the three-dimensional spectrum of the dynamic model decreases and, with it, the projected component variances, so that the two formulations decay together. Throughout the core of the boundary layer ($0.2 \le z/z_i \le 0.6$) and for all the times considered, K_x and K_z obtained from the dynamic model differ from the scale-evolution values by less than about 11% (Table 1); the largest departures, up to about 20%, occur near the top of the layer ($z/z_i = 0.7$) at the latest times,

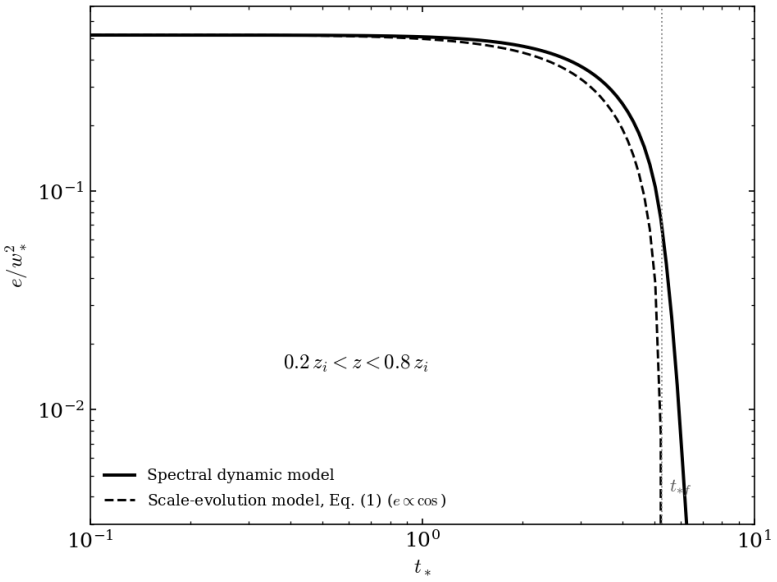


Fig. 5 Temporal evolution of the decay of the mean turbulent kinetic energy in the central region of the CBL ($0.2 \le z/z_i \le 0.8$). The solid line is the spectral dynamic model of Sect. 2.3; the dashed line is the scale-evolution model, Eq. (1), for which $e \propto \cos(\pi t/2\tau_f)$ and vanishes at $t_* \approx 5.3$. Both models are obtained from the same initial spectrum of Degrazia et al. [24] with the micrometeorological parameters of Nieuwstadt and Brost [10].

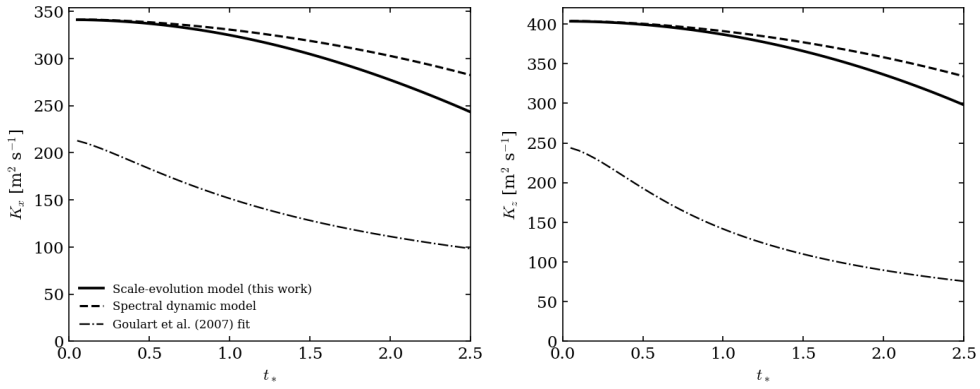


Fig. 6 Temporal evolution of the longitudinal (left) and vertical (right) eddy diffusivities at $z/z_i = 0.5$, calculated with the same expressions (24)–(26) from the scale-evolution model (solid line) and from the spectral dynamic model (dashed line). The dash-dotted line shows the algebraic fits of Goulart et al. [21], fitted to the abrupt shut-off LES of Nieuwstadt and Brost [10] and employed in the Lagrangian dispersion simulations of Carvalho et al. [3].

where the dissipation function (4) decreases rapidly and the component decomposition is most sensitive to the shape of the evolving spectrum. The discrepancy grows slowly as the decay proceeds and remains small over the range of times that controls

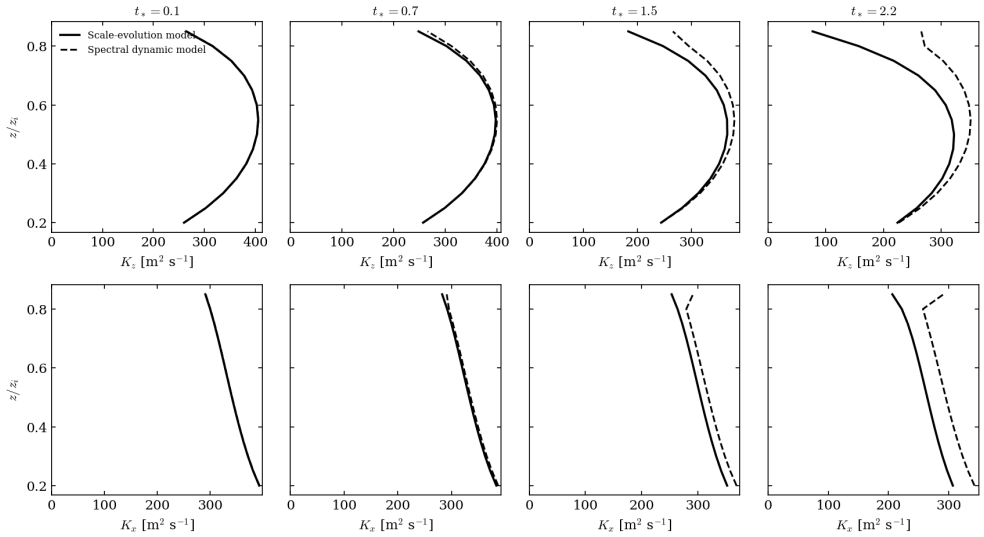


Fig. 7 Vertical profiles of K_z (top) and K_x (bottom) at $t_* = 0.1$, 0.7, 1.5 and 2.2, calculated with the same expressions (24)–(26) from the scale-evolution model (solid lines) and from the spectral dynamic model (dashed lines).

Table 1 Eddy diffusivities [m^2 s^{-1}] obtained from the spectral dynamic model (dyn) and from the scale-evolution model (scale) with the same expressions (24)–(26) and the micrometeorological parameters of Nieuwstadt and Brost [10]. The scale-evolution values are evaluated at fixed heights $z = (z/z_i)\, z_i(t_0)$, with $z_i(t)$ given by Eq. (12).

		K_x		K_z	
z/z_i	t_*	dyn	scale	dyn	scale
0.25	0.1	381	381	303	303
0.25	0.7	376	372	299	299
0.25	1.5	357	341	284	282
0.25	2.2	332	298	264	258
0.5	0.1	341	341	404	403
0.5	0.7	336	333	397	395
0.5	1.5	319	305	377	366
0.5	2.2	295	264	349	322
0.7	0.1	315	315	378	378
0.7	0.7	310	307	372	367
0.7	1.5	293	279	352	325
0.7	2.2	271	240	325	260

the dispersion. Both formulations decay together towards zero, following the product $w_*(t)z_i(t) \propto \cos(\pi t/2\tau_f)$, until the heat flux vanishes at $t_* \to \tau_f w_*/z_i \approx 5.3$. The dash-dotted lines in Fig. 6 show the algebraic expressions of Goulart et al. [21] (Sect. 3.3), evaluated with the same micrometeorological parameters. They have the same order of magnitude as both models, but start from lower values at $t_* \to 0$ ($K_z = 245\ \mathrm{m^2\,s^{-1}}$ against $404\ \mathrm{m^2\,s^{-1}}$ at $z/z_i = 0.5$). This initial offset is not a deficiency of one of the formulations, but a direct consequence of their different structures: being height-independent, the expressions of Goulart et al. [21] represent an effective bulk value for the whole convective layer — at $t_* = 0$ they are, in fact, close to the vertical average of the profiles (24)–(26) (e.g. $K_z \approx 0.094\, w_* z_i \approx 292\ \mathrm{m^2\,s^{-1}}$) — and therefore lie below the mid-layer maximum at which the comparison of Fig. 6 is carried out. Their faster decay, in turn, is explained by the fact that they were fitted to the abrupt shut-off scenario of Nieuwstadt and Brost [10], whereas here the surface heat flux decreases gradually with the external time scale τ_f.

With the source–sink equilibrium calibration, the agreement between the two formulations extends over most of the depth of the convective layer, degrading only in the upper region $z/z_i \gtrsim 0.7$ at the latest times. The direct interaction with the capping inversion and the entrainment zone ($z/z_i \to 1$) remains, as expected, the least reliable region for both formulations — and, in general, for convective similarity-based parameterizations. This has little practical importance for dispersion models whose purpose is the calculation of the concentration of contaminants near the surface, released from sources located inside the growing SBL or in the core of the residual layer, since the transport towards the ground is controlled by the diffusivities in the lower and middle portions of the boundary layer. The close agreement found here — together with the equivalence of the TKE decay shown in Fig. 5 — indicates that the scale-evolution model, with its much simpler mathematical formalism, reproduces the eddy diffusivities of the classical spectral dynamic model in the times and heights that control the dispersion during the sunset transition.

3.2 The Eulerian dispersion model

In order to investigate the influence of the decaying convective turbulence on the dispersion of contaminants during the sunset transition period, the eddy diffusivities derived in Sect. 2.2 are incorporated in a Eulerian dispersion model. The concentration field $\bar{c}(x, y, z, t)$ of a passive and non-reactive contaminant is obtained from the time-dependent advection–diffusion equation, which is derived from the continuity equation employing the first-order (gradient-transfer or K-theory) closure of the turbulence [35, 36],

$$\frac{\partial \bar{c}}{\partial t} + U\frac{\partial \bar{c}}{\partial x} = \frac{\partial}{\partial x}\left(K_x(z,t)\,\frac{\partial \bar{c}}{\partial x}\right) + \frac{\partial}{\partial y}\left(K_y(z,t)\,\frac{\partial \bar{c}}{\partial y}\right) + \frac{\partial}{\partial z}\left(K_z(z,t)\,\frac{\partial \bar{c}}{\partial z}\right) + S, \quad (38)$$

where U is the mean wind speed in the x-direction and S is the source term, representing a continuous point source of strength Q located at $(0, 0, H_s)$,

$$S = Q\,\delta(x)\,\delta(y)\,\delta(z - H_s). \quad (39)$$

Differently from the classical steady-state formulations, in Eq. (38) the eddy diffusivities K_x, K_y and K_z depend explicitly on the time and on the height, so that the equation is able to describe the dispersion in the evolving turbulence that characterizes the decaying CBL. The time dependence of the eddy diffusivities is provided by the scale-evolution model through the expressions (24)–(26), whose vertical profiles, at each dimensionless time t_*, can be evaluated directly from the closed forms or through the polynomial fits presented in Appendix A for the reference scenario.

For the crosswind-integrated concentration, $\bar{c}^{\,y}(x,z,t) = \int_{-\infty}^{\infty} \bar{c}\,\mathrm{d}y$, Eq. (38) reduces to the two-dimensional problem

$$\frac{\partial \bar{c}^{\,y}}{\partial t} + U\frac{\partial \bar{c}^{\,y}}{\partial x} = \frac{\partial}{\partial x}\left(K_x(z,t)\,\frac{\partial \bar{c}^{\,y}}{\partial x}\right) + \frac{\partial}{\partial z}\left(K_z(z,t)\,\frac{\partial \bar{c}^{\,y}}{\partial z}\right) + Q\,\delta(x)\,\delta(z-H_s). \quad (40)$$

Equation (40) is subject to zero-flux boundary conditions at the ground and at the top of the boundary layer,

$$K_z\,\frac{\partial \bar{c}^{\,y}}{\partial z} = 0 \quad \text{at } z = 0 \text{ and } z = z_i, \quad (41)$$

and to a zero initial concentration, $\bar{c}^{\,y}(x,z,t_0) = 0$.

The simulations start at the moment of the sunset transition, when the surface heat flux progressively decreases: near the ground a shear-dominated SBL develops and grows, while above it, in the residual layer, the convective eddies decay. In the surface SBL, where the turbulence is continuously sustained by the mechanical forcing associated to the wind shear, the turbulent transport is represented by the eddy diffusivities derived by Degrazia et al. [24],

$$K_i = C_i\,\frac{(1-z/h)^{3/4}\,u_*\,z}{1+3.7\,\dfrac{z}{\Lambda}}, \qquad \Lambda = L\left(1-\frac{z}{h}\right)^{5/4}, \qquad i = x,y,z, \quad (42)$$

in which $C_x = 4.94$, $C_y = 1.04$ and $C_z = 0.41$, L is the Obukhov length, Λ is the local Obukhov length, u_* is the surface-layer friction velocity and h is the height of the stable layer. In the residual layer ($h < z \leq z_i$) the turbulent transport is represented by the decaying convective eddy diffusivities under evaluation — either the height-dependent expressions (24)–(26) of this work or the height-independent expressions of Goulart et al. [21] presented in Sect. 3.3. The evolution of the SBL height is calculated according to the expression $h = 70\sqrt{t}$, where h is given in meters and t in hours; this parabolic law for the time evolution of the top of the SBL was obtained from Lidar measurements of the nocturnal radiation inversion [37, 38].

In all the simulations the mean wind speed is described by the power law commonly employed in operational dispersion models [39],

$$\frac{U(z)}{U_1} = \left(\frac{z}{z_1}\right)^{\alpha}, \quad (43)$$

where U_1 is the mean wind speed at the reference height z_1 and α is an exponent related to the intensity of the turbulence; the values of U_1, z_1 and α adopted for each scenario are given in Sect. 3.3. During the simulation, new profiles of eddy diffusivities and new values of the SBL height are provided to the model as the transition evolves. The numerical solution of Eqs. (38) and (40) and the analysis of the simulated concentration fields are presented in the next section.

3.3 Dispersion simulations during the sunset transition

In this section the dispersion during the sunset transition is simulated with the two parameterizations of the decaying residual-layer turbulence whose comparison is the central objective of this work. The first is the set of height-dependent eddy diffusivities (24)–(26) derived here from the scale-evolution model, whose supporting spectral balance retains buoyancy and shear production (Sect. 2.3). The second is the set of decaying convective eddy diffusivities derived by Goulart et al. [21] from the isotropic form of the dynamical equation for the energy density spectrum,

$$\frac{K_x}{z_i w_*} = \frac{0.069}{(1+t_*^{1.44})^{1/2}}, \qquad \frac{K_y}{z_i w_*} = \frac{0.079}{(1+t_*^{1.44})^{1/2}}, \qquad \frac{K_z}{z_i w_*} = \frac{0.079}{(1+2\,t_*^{1.7})^{1/2}}, \tag{44}$$

in which z_i and w_* are evaluated at the beginning of the decay. The two formulations differ in three structural aspects. First, the expressions (44) are uniform with height, whereas the diffusivities of this work depend on z/z_i through the reduced frequencies of the spectral peaks and through the dissipation function ψ_ϵ, Eq. (4). For the same reason the two sets do not coincide at the beginning of the decay: the height-independent values (44) are representative of a vertical average of the convective layer, and lie below the mid-layer maximum of the height-dependent profiles (see the discussion of Fig. 6 in Sect. 3.1.2). Second, the temporal decay of (44) is an algebraic law fitted to the abrupt shut-off numerical experiment of Nieuwstadt and Brost [10], in which the residual turbulence decays inertially and never vanishes, whereas in the present model the diffusivities are slaved to the gradually decreasing surface heat flux, $K \propto w_*(t)\, z_i(t) \propto \cos(\pi t/2\tau_f)$, and vanish when the flux vanishes. The description of the extinction of the convective forcing by a gradually decreasing, cosine-shaped surface heat flux is not only the more realistic representation of the sunset transition [11]: it is also supported by direct observations. Anfossi et al. [40] employed the spectral dynamic model with the buoyancy source proportional to $\cos(\pi t/2\tau_f)$ — the same temporal form adopted here in Eqs. (14) and (27) — to describe the decay of the turbulent kinetic energy measured in the surface layer during the total solar eclipse of 11 August 1999, in which the surface heat flux was progressively extinguished in about 80 minutes, and found good agreement between the modelled and the observed decay of the TKE. Third, Eqs. (44) were derived from the isotropic form of the spectral balance, while the present formulation is supported by the non-isotropic balance (27), with buoyancy and shear production. The consequences of these differences are evaluated in two decaying-CBL scenarios: the buoyancy-dominated case of Nieuwstadt and Brost [10] (Sect. 3.3.1), for which the fits (44) were originally constructed, and the

shear-and-buoyancy case SB1 of Moeng and Sullivan [22] (Sect. 3.3.2), in which the mechanical production is relevant.

In both scenarios, Eq. (40) is solved numerically on a regular grid covering a domain of 2000 m in the horizontal direction and the depth of the initial CBL in the vertical direction, with spacings $\Delta x = 25$ m and $\Delta z = 5$ m and a time step $\Delta t = 0.5$ s. The advective term is discretized with a first-order upwind scheme, the longitudinal diffusion term is treated explicitly and the vertical diffusion term is advanced with the Crank–Nicolson method written in conservative (flux) form, which guarantees the discrete conservation of mass under the zero-flux boundary conditions (41). The composite eddy diffusivity profiles — Eq. (42) for $z \leq h(t)$ and one of the two decaying convective parameterizations for $h(t) < z \leq z_i$ — and the SBL height $h(t)$ are updated every 30 s of simulated time. The concentration fields are evaluated for contaminants released from continuous point sources of strength $Q = 1\ \mathrm{g\,s^{-1}}$ located at $H_s = 60$ m (low source, progressively engulfed by the growing SBL) and at $H_s = 120$ m (high source, in the residual layer), and are presented at five instants corresponding to the same dimensionless times $t_* = t w_*/z_i \approx 1.5$, 3.1, 4.6, 6.1 and 8.0 in the two scenarios. The mass balance was monitored during all the simulations: after the plume crosses the domain, the mass in the domain remains constant and equal to $Q\,X_{\max}/U(H_s)$, confirming the conservative character of the numerical scheme.

3.3.1 Buoyancy-dominated scenario: Nieuwstadt and Brost (1986)

The micrometeorological parameters of the first scenario correspond to the LES of a decaying CBL of Nieuwstadt and Brost [10]: $z_i = 1350$ m, $w_* = 2.3\,\mathrm{m\,s^{-1}}$, $u_* = 0.26\,\mathrm{m\,s^{-1}}$ ($u_*/w_* \approx 0.11$) and $L = 4.8$ m for the stable surface layer; the external time scale is $\tau_f = 3100$ s, so that the heat flux vanishes at $t_* = \tau_f w_*/z_i \approx 5.3$. For the wind profile (43), the power-law profile [39] was used. An exponent of $\alpha = 0.07$ is adopted, with $U_1 = 3.6\,\mathrm{m\,s^{-1}}$ at $z_1 = 10$ m—corresponding to run 16 of the Prairie Grass experiment ($L = -5$ m, $h = 1060$ m, and $w_* = 2.03\,\mathrm{m\,s^{-1}}$), the micrometeorological conditions of which are similar to those of this scenario. At the top of the domain, the profile yields $U(z_i) \approx 5\,\mathrm{m\,s^{-1}}$, consistent with the mean wind from the LES simulation by Nieuwstadt and Brost [10].

Figures 8 and 10 present the crosswind-integrated concentration fields obtained with the eddy diffusivities of this work for the low and the high source, respectively, at the times $t = 0.25$, 0.50, 0.75, 1.00 and 1.31 h after the beginning of the transition, corresponding to SBL heights $h \approx 35$, 50, 60, 70 and 80 m. Figures 9 and 11 compare, at the same times, the vertical profiles of the crosswind-integrated concentration at $x = 1000$ m obtained with the diffusivities of this work (solid lines) and with the expressions (44) of Goulart et al. [21] (dashed lines).

In the initial stage of the transition ($t = 0.25$ h, $h \approx 35$ m), the low source is still located above the shallow SBL, in the region where the decaying convective eddies of the residual layer dominate the transport. The large eddy diffusivities inherited from the convective regime promote an intense vertical mixing: the contaminant is rapidly spread through a deep layer and penetrates the stable layer, reaching the surface at short distances from the source (Fig. 8, first panel). As the transition advances, the SBL grows and progressively decouples the source region from the surface. When the

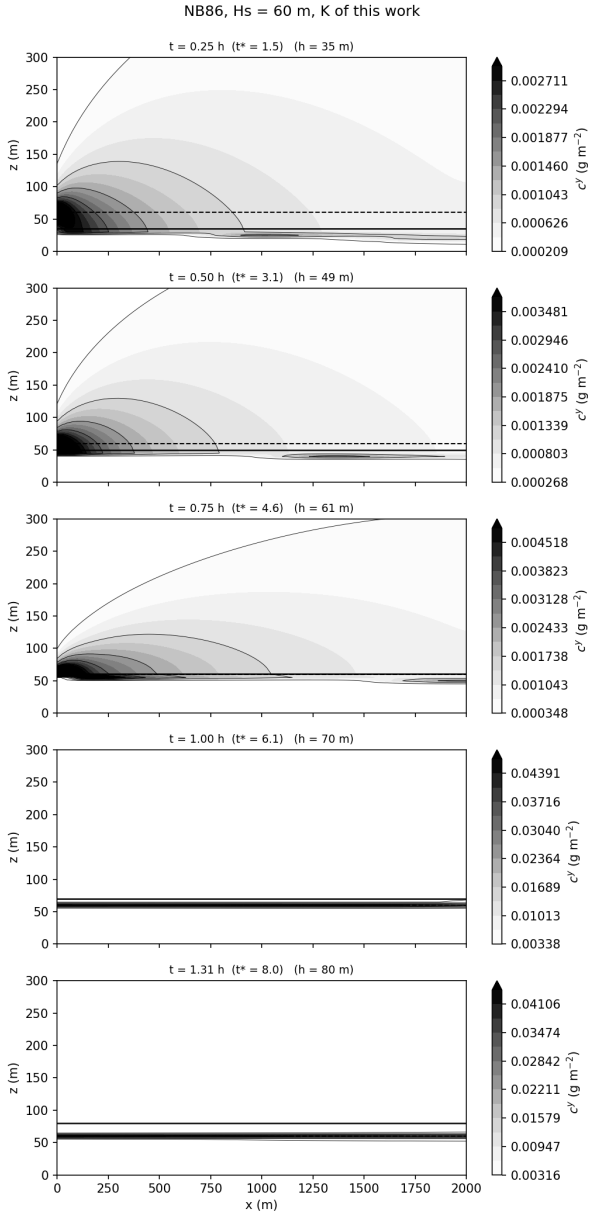


Fig. 8 Buoyancy-dominated scenario [10]: crosswind-integrated concentration fields obtained with the eddy diffusivities of this work for the low source ($H_s = 60$ m) at $t = 0.25$, 0.50, 0.75, 1.00 and 1.31 h ($t_* \approx 1.5$–8.0) after the beginning of the sunset transition. The dashed line indicates the source height and the solid line the top of the growing SBL, $h(t)$.

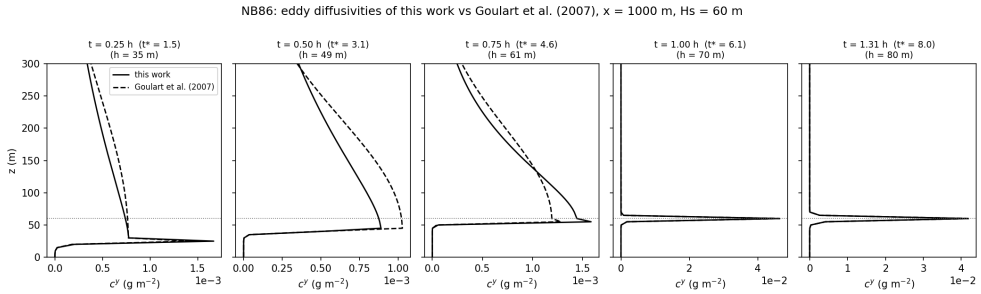


Fig. 9 Buoyancy-dominated scenario: vertical profiles of the crosswind-integrated concentration at $x = 1000$ m for the low source ($H_s = 60$ m), obtained with the eddy diffusivities of this work (solid lines) and with the expressions (44) of Goulart et al. [21] (dashed lines). The dotted line indicates the source height.

stable layer engulfs the source ($t \gtrsim 1$ h, $h \geq 70$ m), the vertical exchange around the emission height is drastically reduced: the plume assumes the form of a thin, elevated ribbon centred at the source height, which travels along the whole domain practically without touching the ground (Fig. 8, last panels). The vertical profiles of Fig. 9 clearly show this regime change: the smooth, deep profiles of the initial times are replaced by a sharp concentration peak at $z \approx H_s$, more than one order of magnitude higher, while the concentration below the peak collapses. The same sequence — fumigation-like ground impact followed by the formation of a long-lived elevated plume — was obtained by Carvalho et al. [3], who simulated the sunset dispersion for this same scenario with a Lagrangian particle model and the eddy diffusivities (44) in the residual layer.

As regards the comparison between the two parameterizations, Fig. 9 shows that in this buoyancy-dominated scenario both sets of eddy diffusivities produce the same sequence of dispersion regimes, with moderate quantitative differences during the phase in which the heat flux is still active ($t_* \lesssim 5.3$). Since the height-dependent diffusivities of this work are larger than (44) in the middle of the residual layer (Fig. 6), the plume spreads over a deeper layer — for the low source at $t_* = 1.5$ the mean plume height at $x = 1000$ m is approximately 259 m against 207 m with Eqs. (44) — and the profile maxima differ by roughly 15–25%, without changing the position of the maximum. Once the SBL engulfs the low source ($t_* \gtrsim 6$), the two solutions become indistinguishable, because the transport around the emission height is then controlled by the stable-layer parameterization (42), common to both simulations.

For the high source (Figs. 10 and 11), located in the residual layer during the whole simulated period, the concentration maximum remains elevated at all times and the ground-level concentrations are systematically smaller than those produced by the low source, in agreement with the high-source Lagrangian simulations of Carvalho et al. [3]. The comparison between the two parameterizations, however, reveals the consequence of their different temporal forms at the late stages of the transition. With the diffusivities of this work, which vanish together with the surface heat flux at $t_* \approx 5.3$, the residual-layer mixing ceases and the plume freezes into a thin, concentrated ribbon at the emission height (Fig. 11, last panels). With the algebraic expressions

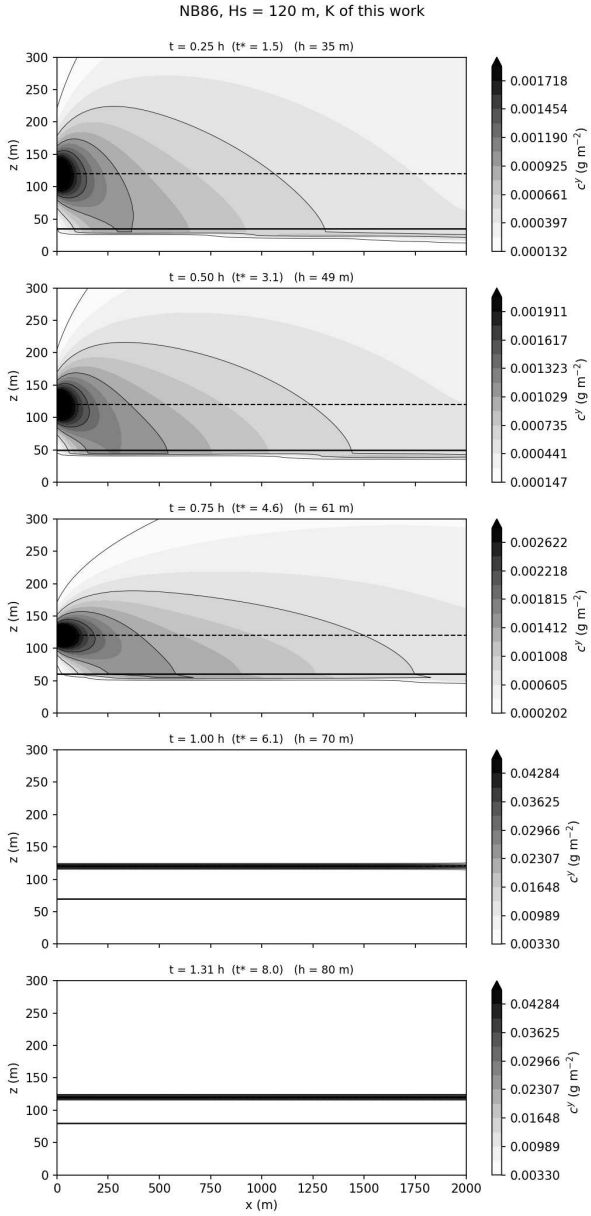


Fig. 10 The same as Fig. 8, but for the high source ($H_s = 120$ m).

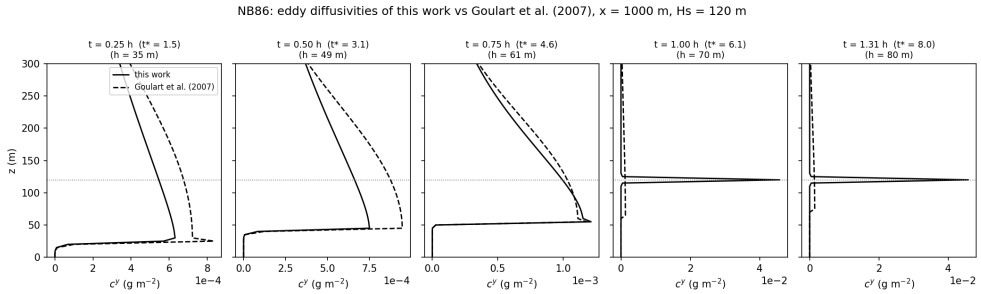


Fig. 11 The same as Fig. 9, but for the high source ($H_s = 120$ m).

(44), which decay but never vanish ($K_z \approx 29$ m^2 s^{-1} at $t_* = 8$ for this scenario), the elevated plume continues to dilute, and the peak concentration at $x = 1000$ m is more than one order of magnitude smaller. The two behaviours bracket the physics of the residual layer in this scenario: expressions (44) were fitted to the inertial decay that follows the abrupt shut-off of the heat flux in the experiment of Nieuwstadt and Brost [10], and therefore retain a residual mixing after the flux vanishes, whereas the present model, being slaved to the flux, switches the residual-layer transport off at $t = \tau_f$. For emissions injected into the residual layer during the evening transition — which can be transported over long distances with little dilution and remain available for fumigation towards the surface on the following morning — the diffusivities of this work therefore provide the more conservative (least diffusive) estimate of the late-stage concentrations.

3.3.2 Shear-and-buoyancy scenario: Moeng and Sullivan (1994), case SB1

The second scenario adopts the initial data of the intermediate simulation SB1 of Moeng and Sullivan [22], in which turbulence is produced by strong shear and moderate convection: $z_i = 498$ m, $w_* = 0.94\,\mathrm{m\,s^{-1}}$, $u_* = 0.59\,\mathrm{m\,s^{-1}}$ ($u_*/w_* \approx 0.63$, $-z_i/L \approx 1.6$), surface heat flux $\overline{(w\theta)}_0(t_0) = 0.05$ K m s^{-1} and geostrophic wind $U_g = 15\,\mathrm{m\,s^{-1}}$ (their Tables 1 and 2). The external time scale is taken as $\tau_f = 5.28\,z_i/w_* \approx 2800$ s, so that the surface heat flux vanishes at the same dimensionless time $t_* \approx 5.3$ as in the previous scenario. For the wind profile (43) the LES data provide two anchor points: the mean wind at the first grid level, $U_1 = 8.1\,\mathrm{m\,s^{-1}}$ at $z_1 \approx 10$ m, and the geostrophic wind at the top of the layer; the exponent $\alpha = 0.157$ is then obtained by requiring $U(z_i) = U_g$. For the stable surface layer that grows after the transition, a nearly neutral SBL is assumed ($u_* = 0.5\,\mathrm{m\,s^{-1}}$ and $L \approx 950$ m in Eq. 42), consistent with the strong geostrophic forcing of this scenario — in contrast with the strongly stable, weak-wind SBL ($L = 4.8$ m) of the previous case. Since the polynomial fits of Appendix A refer to the scenario of Sect. 3.3.1, in the dispersion simulations of this scenario the eddy diffusivities of this work are evaluated directly from the closed forms (24)–(26) with the scales of SB1 and the residual-layer treatment described in Appendix A (convective shape in $z/z_i(t_0)$, amplitude decaying with $w_*(t)z_i(t)$).

Table 2 Shear-and-buoyancy scenario (SB1): eddy diffusivities [$m^2\,s^{-1}$] of the spectral dynamic model with shear production (dyn, Sect. 2.3), of the scale-evolution model of this work (Eqs. 24–26) and of the fits of Goulart et al. [21] (Eqs. 44). r is the mechanical fraction of the turbulence production.

			K_x			K_z		
z/z_i	r	t_*	dyn	this work	Eq. (44)	dyn	this work	Eq. (44)
0.12	0.79	0.5	63	62	28	26	25	29
0.12	0.79	1.5	62	56	19	25	24	17
0.12	0.79	3.0	61	38	13	25	20	10
0.12	0.79	4.5	58	13	10	23	11	7
0.25	0.62	0.5	57	56	28	46	45	29
0.25	0.62	1.5	56	51	19	45	42	17
0.25	0.62	3.0	53	35	13	42	33	10
0.25	0.62	4.5	48	12	10	38	14	7
0.5	0.45	0.5	51	50	28	61	60	29
0.5	0.45	1.5	50	46	19	59	55	17
0.5	0.45	3.0	45	31	13	53	38	10
0.5	0.45	4.5	38	5	10	45	0	7

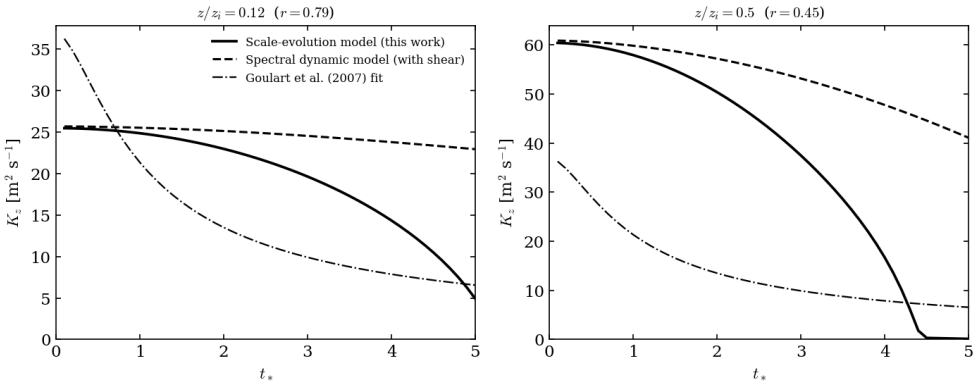


Fig. 12 Shear-and-buoyancy scenario (SB1): temporal evolution of the vertical eddy diffusivity at $z/z_i = 0.12$ (left) and $z/z_i = 0.5$ (right) according to the scale-evolution model of this work (solid line), the spectral dynamic model with shear production (dashed line) and the fits of Goulart et al. [21] (dash-dotted line). r is the mechanical fraction of the turbulence production at each height.

Before discussing the dispersion, it is instructive to compare the three descriptions of the residual-layer diffusivities in this scenario (Table 2 and Fig. 12). Two results stand out. First, during the phase in which the buoyant production is still active ($t_* \lesssim 1.5$), the diffusivities of this work agree with the spectral dynamic model — now with a substantial mechanical source, $r \approx 0.45$–0.8 — to within about 10% at all heights, confirming that the height dependence and the magnitude of Eqs. (24)–(26) correctly represent the non-isotropic turbulence of the sheared CBL. The fits (44), constructed for the strongly convective scenario of Nieuwstadt and Brost, underestimate the diffusivities by a factor of about 2 to 3 over most of the layer (only for the vertical component at the lowest level, where K_z is small, are they comparable): being height-independent and blind to the scenario parameters, they cannot respond to the change of regime. Second, at the late stages ($t_* \gtrsim 3$) the stationary mechanical source sustains the turbulence of the residual layer, and the dynamic model departs from both algebraic parameterizations: while the diffusivities of this work decay with the heat flux and those of Goulart et al. [21] decay algebraically, the dynamic K_z remains nearly constant (≈ 23–$45\ \mathrm{m^2\,s^{-1}}$). (In Table 2 the closed forms of this work are evaluated at fixed heights $z = (z/z_i)\, z_i(t_0)$; the values at $z/z_i = 0.5$ and $t_* = 4.5$ vanish because that level then lies above the shrinking inversion height $z_i(t)$ of Eq. 12.) In a strongly sheared scenario, therefore, both operational parameterizations underestimate the late-time mixing of the residual layer — an aspect further discussed below.

The consequences for the dispersion are shown in Figs. 13–16. The overall sequence of regimes is the same as in the previous scenario — deep mixing while the source lies in the residual layer, followed by the decoupling produced by the growing SBL — but the quantitative differences between the two parameterizations are now large. With the diffusivities of this work the contaminant released at 120 m is spread through a deep portion of the residual layer, reaching $z \approx 250$–300 m, and is entrained into the SBL, producing ground-level concentrations at $x = 1000$ m that are 2 to 5 times higher than those obtained with Eqs. (44) during the active phase of the transition ($t_* \lesssim 4.6$). With the height-independent fits, the weak diffusivities confine the plume around the emission height, where the concentration maximum remains up to about 55% higher and the vertical spreading is visibly truncated (Figs. 14 and 16, first panels). In a scenario in which the LES data [22] and the spectral dynamic model with shear indicate an intense, shear-sustained turbulent transport in the residual layer, the parameterization proposed here — supported by the dynamic model to within 10% during the active phase — provides the more realistic description, while the isotropic, height-independent expressions substantially underestimate both the vertical spreading of elevated plumes and their impact at the surface.

It should be noted, finally, that after the extinction of the buoyant production ($t_* \gtrsim 5.3$) the simulations with the diffusivities of this work also freeze the elevated plume (Figs. 14 and 16, last panels), whereas the spectral dynamic model with the stationary mechanical source indicates that the residual-layer mixing persists (Fig. 12). In strongly sheared scenarios the slaving of the eddy diffusivities to the surface heat flux is therefore a conservative approximation, valid for the phase $t_* \lesssim 5$ that concentrates

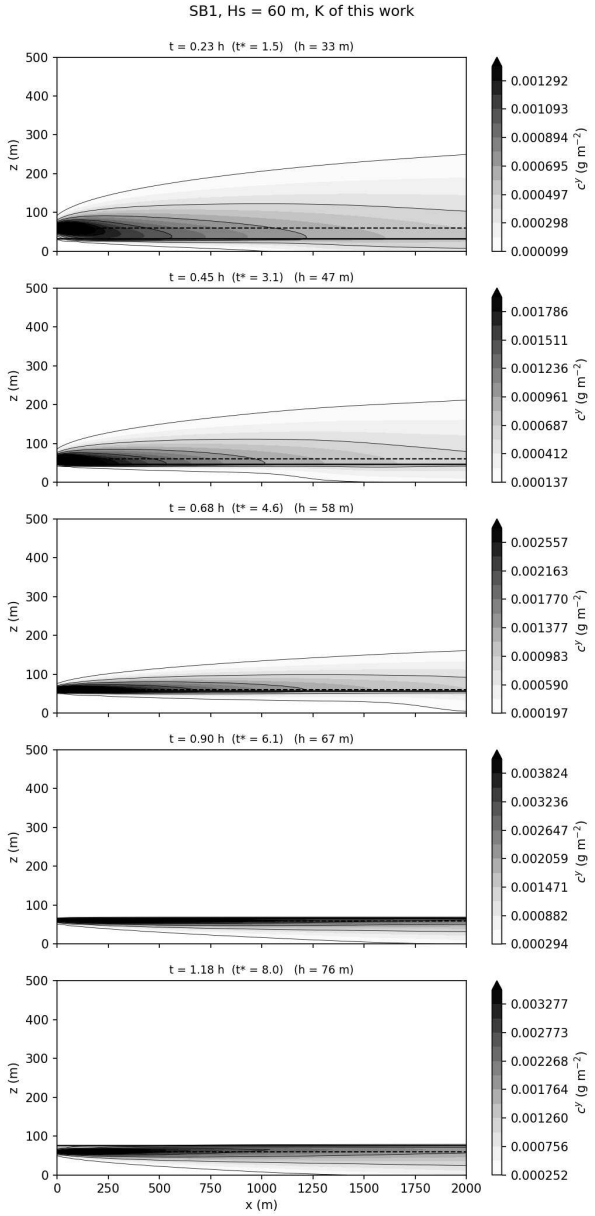


Fig. 13 Shear-and-buoyancy scenario (SB1): crosswind-integrated concentration fields obtained with the eddy diffusivities of this work for the low source ($H_s = 60$ m) at $t = 0.23$, 0.45, 0.68, 0.90 and 1.18 h ($t_* \approx 1.5$–8.0). The dashed line indicates the source height and the solid line the top of the growing SBL, $h(t)$.

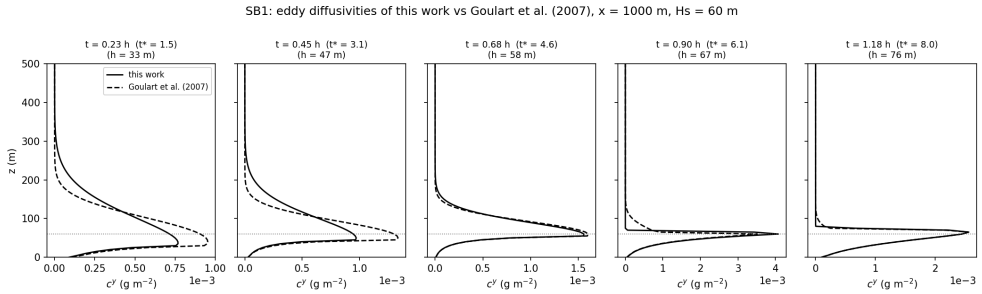


Fig. 14 Shear-and-buoyancy scenario (SB1): vertical profiles of the crosswind-integrated concentration at $x = 1000$ m for the low source ($H_s = 60$ m), obtained with the eddy diffusivities of this work (solid lines) and with the expressions (44) of Goulart et al. [21] (dashed lines). The dotted line indicates the source height.

the transition; the extension of the scale-evolution model to include a mechanical contribution to the evolution of the characteristic scales is a natural development of this work.

4 Conclusion

In this work a simple model for the decay of the turbulent kinetic energy in the convective boundary layer during the afternoon–sunset transition was proposed. Instead of solving a differential equation for the energy density spectrum, the decay is described as a succession of quasi-stationary states, characterized at each instant by the time evolution of the characteristic scales of the convective flow — the convective velocity scale $w_*(t)$ and the inversion height $z_i(t)$ — which decrease as the surface heat flux weakens. The evolving three-dimensional energy density spectrum is constructed from the one-dimensional convective spectra of Degrazia et al. [24] by means of the spectral tensor formulation of Kristensen et al. [23]. At $t = t_0$ the velocity variances obtained from the model agree with observational and large-eddy simulation results for the fully developed CBL, and during the decay it reproduces the behaviour of the classical spectral dynamic model, both formulations vanishing together with the surface heat flux at $t_* \approx 5.3$. The main advantage of the proposed approach is the simplicity of its mathematical formalism, since no differential equation has to be solved.

From the evolving spectrum, time- and height-dependent eddy diffusivities for the longitudinal, lateral and vertical directions were derived by means of Taylor's statistical diffusion theory, and were expressed as polynomial functions of the dimensionless height for a sequence of dimensionless times (Appendix A), in a form suitable for direct use in air quality models. In the range of times and heights that control the transport of pollutants towards the ground, these decaying eddy diffusivities agree with those of the spectral dynamic model — solved here retaining both the buoyancy and the mechanical (shear) production terms [18] — within about 11%.

We compared the height-dependent eddy diffusivities proposed in this work (Eqs. 24, 25, 26)— based on the anisotropic spectral balance—with the height-independent expressions derived by Goulart et al. [21] from the isotropic form of the spectral equation, which depend solely on dimensionless time. Both sets were incorporated in a

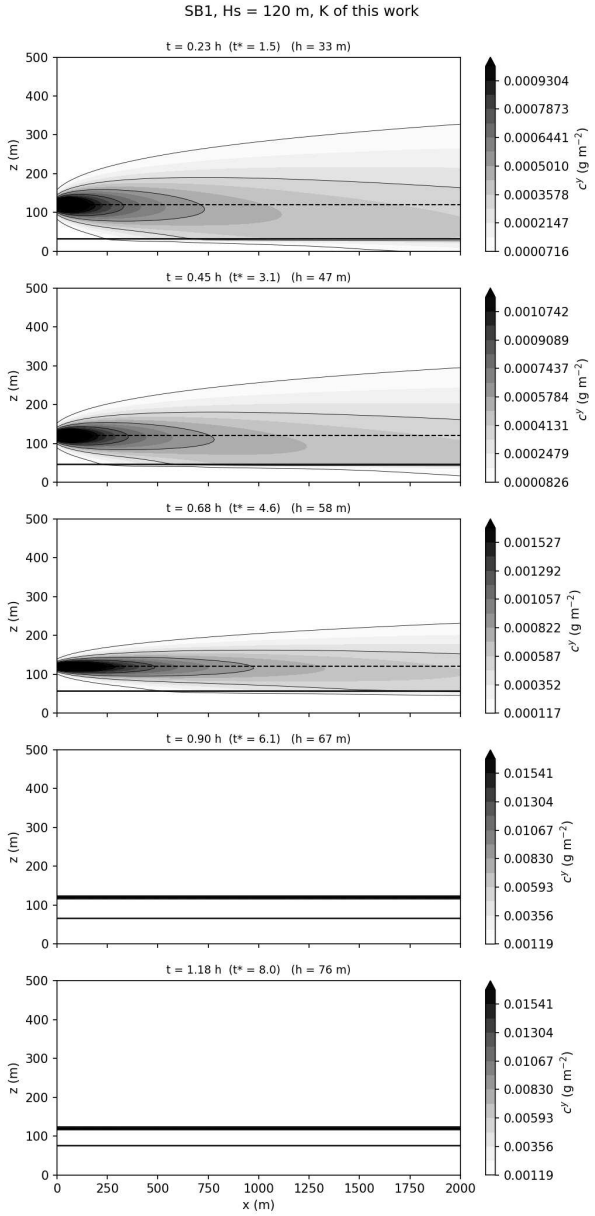


Fig. 15 The same as Fig. 13, but for the high source ($H_s = 120$ m).

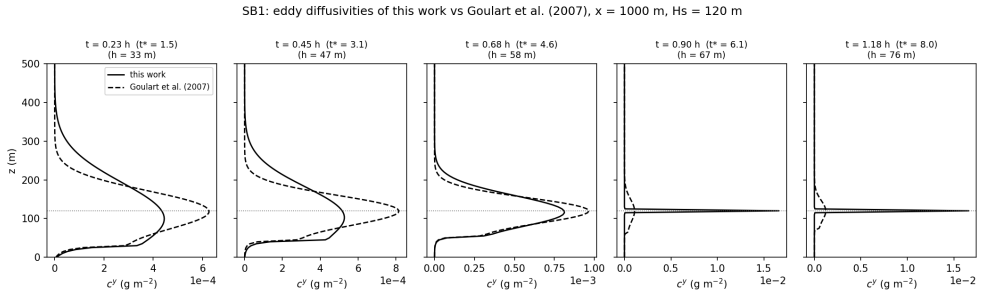


Fig. 16 The same as Fig. 14, but for the high source ($H_s = 120$ m).

Eulerian dispersion model based on the time-dependent advection–diffusion equation, and the dispersion during the sunset transition was simulated for two decaying-CBL scenarios. In the buoyancy-dominated scenario of Nieuwstadt and Brost [10] — the scenario for which the isotropic fits were originally constructed, and for which Carvalho et al. [3] performed a similar (Lagrangian) simulation — the two parameterizations produce the same sequence of dispersion regimes, namely the fumigation-like ground impact of the initial stage followed by the formation of long-lived, ribbon-like elevated plumes, with moderate quantitative differences (15–25% in the profile maxima and a deeper vertical spreading with the present formulation) and one structural difference at the late stages, when the algebraic fits retain a residual mixing whereas the present diffusivities vanish with the heat flux. In the shear-and-buoyancy scenario SB1 of Moeng and Sullivan [22], in contrast, the advantage of the formulation proposed here is evident: its diffusivities agree within about 10% with the spectral dynamic model with shear production during the active phase of the transition, while the height-independent expressions — blind to the height and to the scales of the scenario — underestimate the residual-layer diffusivities by a factor of 2 to 3, truncating the vertical spreading of elevated plumes and underestimating their ground-level impact by a factor of 2 to 5. The spectral dynamic model with the stationary mechanical source also indicates that, in strongly sheared scenarios, the residual-layer mixing persists after the extinction of the buoyant production; the slaving of the proposed diffusivities to the surface heat flux is then a conservative approximation, and the extension of the scale-evolution model to include a mechanical contribution to the evolution of the characteristic scales is a natural development of this work, together with the extension of the Eulerian simulations to the fully three-dimensional concentration field and a more detailed treatment of the interface between the growing stable boundary layer and the residual layer.

Acknowledgements. The authors gratefully acknowledge the partial financial support of the Brazilian research agency CNPq (Conselho Nacional de Desenvolvimento Científico e Tecnológico).

Declarations

Funding. This work was partially supported by the Brazilian research agency CNPq (Conselho Nacional de Desenvolvimento Científico e Tecnológico).
Conflict of interest. The authors declare that they have no conflict of interest.
Ethics approval and consent to participate. Not applicable.
Consent for publication. All authors have read and approved the final version of the manuscript and consent to its publication.
Data availability. The micrometeorological data used in this work were taken from the published literature cited in the text. No new measurement data were generated.
Materials availability. Not applicable.
Code availability. The codes used to generate the results of this work are available from the corresponding author on reasonable request.
Author contribution. All authors contributed to the conception and design of the study, to the development of the model, to the analysis of the results and to the writing of the manuscript. All authors read and approved the final manuscript.

Appendix A Polynomial fits for the decaying eddy diffusivities

In this appendix we present the expressions for the temporal evolution of the vertical profiles of the eddy diffusivity components (24)–(26) as functions of the dimensionless height, in the longitudinal (x), lateral (y) and vertical (z) directions, shown in Figures 2, 3 and 4. The profiles were generated with the micrometeorological parameters of the buoyancy-dominated scenario of Sect. 3.3.1 ($z_i = 1350$ m, $w_* = 2.3\,\mathrm{m\,s^{-1}}$, $u_* = 0.26\,\mathrm{m\,s^{-1}}$ and $\tau_f = 3100$ s); for other scenarios (such as the sheared case of Sect. 3.3.2) the eddy diffusivities should be evaluated directly from the closed forms (24)–(26) with the corresponding scales w_* and z_i, the polynomial fits below being provided for the operational use of the reference scenario. As the inversion height decreases during the decay (Eq. 12), the residual-layer diffusivity profiles retain the convective shape as a function of $z/z_i(t_0)$ while their amplitude decays in proportion to $w_*(t)\,z_i(t) \propto \cos(\pi t/2\tau_f)$; the coefficients tabulated below are normalized by the initial value $w_*(t_0)\,z_i(t_0)$, so that the temporal decay is contained in the coefficients themselves. The longitudinal and lateral components are fitted by third-degree polynomials,

$$\frac{K_{x,y}}{w_* z_i} = a_0 + a_1\left(\frac{z}{z_i}\right) + a_2\left(\frac{z}{z_i}\right)^2 + a_3\left(\frac{z}{z_i}\right)^3, \tag{A1}$$

and the vertical component by a sixth-degree polynomial,

$$\frac{K_z}{w_* z_i} = b_0 + b_1\left(\frac{z}{z_i}\right) + b_2\left(\frac{z}{z_i}\right)^2 + b_3\left(\frac{z}{z_i}\right)^3 + b_4\left(\frac{z}{z_i}\right)^4 + b_5\left(\frac{z}{z_i}\right)^5 + b_6\left(\frac{z}{z_i}\right)^6, \tag{A2}$$

with the coefficients, for each dimensionless time t_*, given in Tables A1, A2 and A3. The fits are valid for $0.05 \le z/z_i \le 0.98$, with maximum errors of a few percent (very close to the inversion the dissipation function (4) vanishes with infinite slope and the

polynomials extrapolate smoothly). Within the scale-evolution model the surface heat flux (14) vanishes at $t_* = \tau_f w_*/z_i \approx 5.3$; beyond this time the residual-layer eddy diffusivities are zero, the convective turbulence having completely decayed.

Table A1 Coefficients of the polynomial fit (A1) for the longitudinal eddy diffusivity $K_x/w_* z_i$.

t_*	a_0	a_1	a_2	a_3
0.1	0.1541	−0.1803	0.2599	−0.1554
0.5	0.1525	−0.1784	0.2572	−0.1538
1.0	0.1474	−0.1724	0.2486	−0.1487
1.5	0.1391	−0.1627	0.2346	−0.1403
2.0	0.1277	−0.1494	0.2154	−0.1288
2.5	0.1135	−0.1327	0.1914	−0.1145
3.0	0.0968	−0.1132	0.1632	−0.0976
3.5	0.0779	−0.0911	0.1314	−0.0786
4.0	0.0574	−0.0671	0.0967	−0.0578
4.5	0.0355	−0.0415	0.0599	−0.0358
5.0	0.0129	−0.0151	0.0217	−0.0130

Table A2 Coefficients of the polynomial fit (A1) for the lateral eddy diffusivity $K_y/w_* z_i$.

t_*	a_0	a_1	a_2	a_3
0.1	0.1780	−0.2082	0.3001	−0.1795
0.5	0.1761	−0.2059	0.2969	−0.1776
1.0	0.1702	−0.1991	0.2871	−0.1717
1.5	0.1606	−0.1879	0.2709	−0.1620
2.0	0.1475	−0.1725	0.2487	−0.1487
2.5	0.1311	−0.1533	0.2210	−0.1322
3.0	0.1118	−0.1307	0.1885	−0.1127
3.5	0.0900	−0.1052	0.1518	−0.0907
4.0	0.0662	−0.0775	0.1117	−0.0668
4.5	0.0410	−0.0480	0.0692	−0.0414
5.0	0.0149	−0.0174	0.0251	−0.0150

Appendix B Closed form of the three-dimensional energy density spectrum

In this appendix the integrals of Eq. (2) are reduced to a closed algebraic form. Substituting the definition (9) of $g'''(S, z)$, with the third derivative given by (10)–(11),

Table A3 Coefficients of the polynomial fit (A2) for the vertical eddy diffusivity $K_z/w_* z_i$.

t_*	b_0	b_1	b_2	b_3	b_4	b_5	b_6
0.1	−0.0035	0.5384	−0.2701	−1.9774	4.6045	−4.0876	1.1943
0.5	−0.0034	0.5327	−0.2673	−1.9564	4.5557	−4.0442	1.1817
1.0	−0.0033	0.5150	−0.2584	−1.8914	4.4043	−3.9098	1.1424
1.5	−0.0031	0.4860	−0.2438	−1.7846	4.1557	−3.6891	1.0779
2.0	−0.0029	0.4462	−0.2238	−1.6385	3.8153	−3.3870	0.9896
2.5	−0.0026	0.3965	−0.1989	−1.4561	3.3908	−3.0101	0.8795
3.0	−0.0022	0.3381	−0.1696	−1.2417	2.8914	−2.5668	0.7500
3.5	−0.0018	0.2722	−0.1366	−0.9998	2.3281	−2.0668	0.6039
4.0	−0.0013	0.2004	−0.1005	−0.7358	1.7135	−1.5211	0.4445
4.5	−0.0008	0.1241	−0.0623	−0.4557	1.0611	−0.9419	0.2752
5.0	−0.0003	0.0450	−0.0226	−0.1654	0.3852	−0.3420	0.0999

each integral in Eq. (2) becomes a sum of terms of the type

$$I_{1i}^{(n)} = \int_0^{1/k^2} \frac{S^{\frac{20-3n}{6}}}{\left(1+\sqrt{B_i S}\right)^{\frac{14-3n}{3}}}\,\mathrm{d}S, \qquad I_{2i}^{(n)} = \int_0^{1/k^2} \frac{S^{\frac{12-3n}{6}}}{\left(1+\sqrt{B_i S}\right)^{\frac{14-3n}{3}}}\,\mathrm{d}S. \tag{B3}$$

These integrals can be written in algebraic form by means of the changes of variables $\sqrt{B_i S} = (Z^3-1)^{-1}$ in $I_{1i}^{(n)}$ and $\sqrt{B_i S} = Z^3 - 1$ in $I_{2i}^{(n)}$, which give

$$I_{1i}^{(n)} = 6\, B_i^{-\frac{26-3n}{6}} \int_{W_{1i}}^{\infty} \frac{Z^{3n-12}}{(Z^3-1)^5}\,\mathrm{d}Z, \tag{B4}$$

$$I_{2i}^{(n)} = 6\, B_i^{\frac{n}{2}-3} \int_1^{W_{2i}} Z^{3n-12}\left(Z^3-1\right)^{5-n}\,\mathrm{d}Z, \tag{B5}$$

where, evaluating $\sqrt{B_i S}$ at the upper limit $S = k^{-2}$ (and recalling that $B_i = b_i^{-2}$), the limits of integration assume the simple form

$$W_{1i} = (1+b_i k)^{1/3}, \qquad W_{2i} = \left(1+\frac{1}{b_i k}\right)^{1/3}. \tag{B6}$$

Substituting (B4) and (B5) into Eq. (2), the powers of B_i combine into factors independent of the summation index n, and the three-dimensional spectrum assumes the

closed form

$$
\begin{aligned}
E\left(k,z\right) = {} & k^3 \frac{\mathrm{d}}{\mathrm{d}k}\left(\frac{1}{k}\frac{\mathrm{d}E_u}{\mathrm{d}k}\right) \\
& + 12\,k^4 \sum_i m_i A_i B_i^{-\frac{17}{6}} \sum_{n=0}^{3} C_n \int_{W_{1i}}^{\infty} \frac{Z^{3n-12}}{\left(Z^3-1\right)^5}\,\mathrm{d}Z \\
& - \frac{84}{9}\,k^{4/3} \sum_i m_i A_i B_i^{-\frac{3}{2}} \sum_{n=0}^{3} C_n \int_{1}^{W_{2i}} Z^{3n-12}\left(Z^3-1\right)^{5-n}\,\mathrm{d}Z,
\end{aligned}
\tag{B7}
$$

in which the first term is evaluated directly from (6),

$$
k^3 \frac{\mathrm{d}}{\mathrm{d}k}\left(\frac{1}{k}\frac{\mathrm{d}E_u}{\mathrm{d}k}\right) = \frac{5}{3}\,\frac{a_u b_u k}{\left(1+b_u k\right)^{8/3}} + \frac{40}{9}\,\frac{a_u b_u^2 k^2}{\left(1+b_u k\right)^{11/3}}. \tag{B8}
$$

The remaining Z-integrals in (B7) have rational integrands and can be evaluated in elementary form (or numerically at negligible cost); the first integral converges, since its integrand behaves as Z^{3n-27} for large Z. The time evolution of the spectrum is introduced through $w_*(t)$ and $z_i(t)$ in the amplitudes a_i and length scales b_i of Eq. (7). Equation (B7) was verified numerically against the direct integration of Eq. (2), with agreement at machine precision.

References

[1] Stull, R.B.: An Introduction to Boundary Layer Meteorology. Kluwer Academic Publishers, Dordrecht (1988)

[2] Garratt, J.R.: The Atmospheric Boundary Layer. Cambridge University Press, Cambridge (1992)

[3] Carvalho, J.C., Degrazia, G.A., Anfossi, D., Goulart, A.G., Cuchiara, G.C., Mortarini, L.: Simulating the characteristic patterns of the dispersion during sunset PBL. Atmospheric Research **98**(2-4), 274–284 (2010)

[4] Pino, D., Jonker, H.J.J., Vilà-Guerau de Arellano, J., Dosio, A.: Role of shear and the inversion strength during sunset turbulence over land: characteristic length scales. Boundary-Layer Meteorology **121**(3), 537–556 (2006)

[5] Darbieu, C., Lohou, F., Lothon, M., Vilà-Guerau de Arellano, J., Couvreux, F., Durand, P., Pino, D., Patton, E.G., Nilsson, E., Blay-Carreras, E., Gioli, B.: Turbulence vertical structure of the boundary layer during the afternoon transition. Atmospheric Chemistry and Physics **15**(17), 10071–10086 (2015)

[6] Vilà-Guerau de Arellano, J., Gioli, B., Miglietta, F., Jonker, H.J.J., Klein Baltink, H., Hutjes, R.W.A., Holtslag, A.A.M.: Entrainment process of carbon dioxide in

the atmospheric boundary layer. Journal of Geophysical Research: Atmospheres **109**(D18), 18110 (2004)

[7] Casso-Torralba, P., Vilà-Guerau de Arellano, J., Bosveld, F., Soler, M.R., Vermeulen, A., Werner, C., Moors, E.: Diurnal and vertical variability of the sensible heat and carbon dioxide budgets in the atmospheric surface layer. Journal of Geophysical Research: Atmospheres **113**(D12), 12119 (2008)

[8] Monin, A.S., Yaglom, A.M.: Statistical Fluid Mechanics: Mechanics of Turbulence vol. 2. MIT Press, Cambridge, MA (1975)

[9] Cole, G.S., Fernando, H.J.S.: Some aspects of the decay of convective turbulence. Fluid Dynamics Research **23**(3), 161–176 (1998)

[10] Nieuwstadt, F.T.M., Brost, R.A.: The decay of convective turbulence. Journal of the Atmospheric Sciences **43**(6), 532–546 (1986)

[11] Sorbjan, Z.: Decay of convective turbulence revisited. Boundary-Layer Meteorology **82**(3), 501–515 (1997)

[12] Rizza, U., Miglietta, M.M., Degrazia, G.A., Acevedo, O.C., Anfossi, D.: Sunset decay of the convective turbulence with Large-Eddy Simulation under realistic conditions. Physica A: Statistical Mechanics and its Applications **392**(19), 4481–4490 (2013)

[13] Grant, A.L.M.: An observational study of the evening transition boundary-layer. Quarterly Journal of the Royal Meteorological Society **123**(539), 657–677 (1997)

[14] Fitzjarrald, D.R., Freedman, J.M., Czikowsky, M.J., Sakai, R.K., Acevedo, O.C., Moraes, O.L.L.: Momentum and scalar transport during the decay of CBL turbulence. In: 16th Symposium on Boundary Layers and Turbulence, Portland, ME, USA (2004). Paper 4.23

[15] Fernando, H.J.S., Princevac, M., Pardyjak, E.R., Data, A.: The decay of convective turbulence during evening transition period. In: 11th Conference on Mountain Meteorology and MAP Meeting, Bartlett, NH, USA (2004). Paper 10.3

[16] Brazel, A.J., Fernando, H.J.S., Hunt, J.C.R., Selover, N., Hedquist, B.C., Pardyjak, E.: Evening transition observations in Phoenix, Arizona. Journal of Applied Meteorology **44**(1), 99–112 (2005)

[17] Goulart, A., Degrazia, G., Rizza, U., Anfossi, D.: A theoretical model for the study of convective turbulence decay and comparison with large-eddy simulation data. Boundary-Layer Meteorology **107**(1), 143–155 (2003)

[18] Goulart, A.G., Bodmann, B.E.J., de Vilhena, M.T.M.B., Soares, P.M.M., Moreira, D.M.: On the time evolution of the turbulent kinetic energy spectrum

for decaying turbulence in the convective boundary layer. Boundary-Layer Meteorology **138**(1), 61–75 (2011)

[19] Nilsson, E., Lothon, M., Lohou, F., Pardyjak, E., Hartogensis, O., Darbieu, C.: Turbulence kinetic energy budget during the afternoon transition – Part 2: A simple TKE model. Atmospheric Chemistry and Physics **16**(14), 8873–8898 (2016)

[20] Lothon, M., Lohou, F., Pino, D., Couvreux, F., Pardyjak, E.R., Reuder, J., Vilà-Guerau de Arellano, J., Durand, P., Hartogensis, O., Legain, D., Augustin, P., Gioli, B., Lenschow, D.H., Faloona, I., Yagüe, C., Alexander, D.C., Angevine, W.M., Bargain, E., Barrié, J., Bazile, E., Bezombes, Y., Blay-Carreras, E., Boer, A., Boichard, J.L., Bourdon, A., Butet, A., Campistron, B., Coster, O., Cuxart, J., Dabas, A., Darbieu, C., Deboudt, K., Delbarre, H., Derrien, S., Flament, P., Fourmentin, M., Garai, A., Gibert, F., Graf, A., Groebner, J., Guichard, F., Jiménez, M.A., Jonassen, M., Kranenburg, R., Lampert, A., Martin, S.: The BLLAST field experiment: Boundary-Layer Late Afternoon and Sunset Turbulence. Atmospheric Chemistry and Physics **14**(20), 10931–10960 (2014)

[21] Goulart, A.G., Vilhena, M.T., Degrazia, G., Flores, D.T.: Vertical, lateral and longitudinal eddy diffusivities for a decaying turbulence in the convective boundary layer. Ecological Modelling **204**(3-4), 516–522 (2007)

[22] Moeng, C.-H., Sullivan, P.P.: A comparison of shear- and buoyancy-driven planetary boundary layer flows. Journal of the Atmospheric Sciences **51**(7), 999–1022 (1994)

[23] Kristensen, L., Lenschow, D.H., Kirkegaard, P., Courtney, M.: The spectral velocity tensor for homogeneous boundary-layer turbulence. Boundary-Layer Meteorology **47**(1-4), 149–193 (1989)

[24] Degrazia, G.A., Anfossi, D., Carvalho, J.C., Mangia, C., Tirabassi, T., Campos Velho, H.F.: Turbulence parameterisation for PBL dispersion models in all stability conditions. Atmospheric Environment **34**(21), 3575–3583 (2000)

[25] Højstrup, J.: Velocity spectra in the unstable planetary boundary layer. Journal of the Atmospheric Sciences **39**(10), 2239–2248 (1982)

[26] Carson, D.J.: The development of a dry inversion-capped convectively unstable boundary layer. Quarterly Journal of the Royal Meteorological Society **99**(421), 450–467 (1973)

[27] Deardorff, J.W.: Convective velocity and temperature scales for the unstable planetary boundary layer and for Rayleigh convection. Journal of the Atmospheric Sciences **27**(8), 1211–1213 (1970)

[28] Tennekes, H.: Free convection in the turbulent Ekman layer of the atmosphere.

Journal of the Atmospheric Sciences **27**(7), 1027–1034 (1970)

[29] Weil, J.C.: Stochastic modeling of dispersion in the convective boundary layer. In: Dop, H. (ed.) Air Pollution Modeling and Its Application VII, pp. 437–449. Plenum Press, New York (1989)

[30] Degrazia, G.A., Anfossi, D.: Estimation of the Kolmogorov constant c_0 from classical statistical diffusion theory. Atmospheric Environment **32**(20), 3611–3614 (1998)

[31] Pao, Y.H.: Structure of turbulent velocity and scalar fields at large wavenumbers. Physics of Fluids **8**(6), 1063–1075 (1965)

[32] Lenschow, D.H., Wyngaard, J.C., Pennell, W.T.: Mean-field and second-moment budgets in a baroclinic, convective boundary layer. Journal of the Atmospheric Sciences **37**(6), 1313–1326 (1980)

[33] Zhou, B., Sun, S., Sun, J., Zhu, K.: The universality of the normalized vertical velocity variance in contrast to the horizontal velocity variance in the convective boundary layer. Journal of the Atmospheric Sciences **76**(5), 1437–1456 (2019)

[34] Caughey, S.J., Palmer, S.G.: Some aspects of turbulence structure through the depth of the convective boundary layer. Quarterly Journal of the Royal Meteorological Society **105**(446), 811–827 (1979)

[35] Arya, S.P.: Air Pollution Meteorology and Dispersion. Oxford University Press, New York (1999)

[36] Seinfeld, J.H., Pandis, S.N.: Atmospheric Chemistry and Physics: From Air Pollution to Climate Change, 2nd edn. John Wiley & Sons, Hoboken, NJ (2006)

[37] Anfossi, D., Bacci, P., Longhetto, A.: An application of Lidar technique to the study of the nocturnal radiation inversion. Atmospheric Environment **8**(5), 537–541 (1974)

[38] Anfossi, D., Bacci, P., Longhetto, A.: Forecasting of vertical temperature profiles in the atmosphere during nocturnal radiation inversions from air temperature trend at screen height. Quarterly Journal of the Royal Meteorological Society **102**(431), 173–180 (1976)

[39] Panofsky, H.A., Dutton, J.A.: Atmospheric Turbulence: Models and Methods for Engineering Applications. John Wiley and Sons, New York (1984)

[40] Anfossi, D., Schayes, G., Degrazia, G., Goulart, A.: Atmospheric turbulence decay during the solar total eclipse of 11 August 1999. Boundary-Layer Meteorology **111**(2), 301–311 (2004)